SEDIMENTOLOGY
the journal of the
International Association of Sedimentologists

Shark-fins: overturned patterns linked to shear instabilities at the flow-bed boundary. Examples from the deposits of the 2006 pyroclastic currents at Tungurahua volcano (Ecuador)

Journal:	*Sedimentology*
Manuscript ID	Draft
Manuscript Type:	Original Manuscript
Date Submitted by the Author:	n/a
Complete List of Authors:	Douillet, Guilhem; Universität Bern, Institut für Geologie; Ludwig-Maximilians-Universität, Department für Geo und Umweltwissenschaften Chaffaut, Quentin; Universite de Strasbourg Ecole et Observatoire des Sciences de la Terre Schlunegger, Fritz; University of Bern, Institute of Geological Sciences Kueppers, Ulrich; Ludwig-Maximilians-Universität, Department für Geo und Umweltwissenschaften Dingwell, Donald; Ludwig-Maximilians-Universität, Department für Geo und Umweltwissenschaften
Keywords:	shark-fins, convolute lamina, overturned beds, flame structures, flow shearing, pyroclastic currents
Note: The following files were submitted by the author for peer review, but cannot be converted to PDF. You must view these files (e.g. movies) online.	
ANNEX2_Equations.docx	

Shark-fins: overturned patterns linked to shear instabilities at the flow-bed boundary. Examples from the deposits of the 2006 pyroclastic currents at Tungurahua volcano (Ecuador)

Guilhem Amin Douillet[1,2], Quentin Chaffaut[2, 3], Fritz Schlunegger[1], Ulrich Kueppers[2], Donald B Dingwell[2]

[1] Institut für Geologie, Universität Bern, Switzerland

[2] Ludwig-Maximilians-Universität München, Germany

[3] Ecole et Observatoire des Sciences de la Terre, Strasbourg, France

Keywords: 1. shark-fins, 2. convolute laminae, 3. flame structures, 4. overturned beds, 5. flow shearing, 6. pyroclastic currents

Running title: Overturned shark-fins from pyroclastic currents

ABSTRACT

Enigmatic structures grouped under the term "shark-fins" are documented in laminated deposits of pyroclastic currents. They consist of an overturning of a few laminae on a decimeter scale, forming overbent "flames" or convolute laminae, which occur in successive, periodic patterns. More than 200 shark-fins were investigated and measured in cross-laminated deposits from the 2006 pyroclastic currents of Tungurahua volcano (Ecuador). Shark-fins often underlie erosive lines. They occur in periodic repetitions or amalgamated in swarms and can show signs of migration as well as concurrent growth during sedimentation. These shark-fins are interpreted in terms of syn-depositional soft sediment deformation. The patterns are interpreted as due to the reworking of the bed by wave instabilities, which form around a shear horizon between a traction carpet and the bed. A theoretical framework based on two fluid layers separated by a shear horizon is adapted from the Holmboe instability problem. The calculated growth rates of the waves are compared to sedimentation rates in order to infer aspects of the stability and preservation of the sheared interfaces. The good agreement of the physical model with field data supports the process-based interpretation. In particular, such modified Holmboe instabilities seem more adequate than Kelvin-Helmholtz instabilities to explain overturned shark-fins structures. Other incidental overturned patterns are presented and discussed, which likely result from an intraflow event as well as from syn-flow slumping. Such observations on flow-bed interactions contribute to the understanding of a flow rheology, shear partitioning, and the transmission of shear stress out of the flow and into the substrate.

1. INTRODUCTION

1.1. Pyroclastic currents

Pyroclastic currents are flowing mixtures of gas and particles ejected during explosive volcanic eruptions (e.g. Kneller and Buckee 2000, Branney and Kokelaar 2002, Dufek 2016, Palladino 2017). From the analysis of deposits, a range of flow transport processes has been postulated between two end-member behaviors: concentrated granular flow type and dilute, fully turbulent, gas-supported currents (e.g. Sparks 1976, Fisher 1979, Douillet et al. 2013a). The high particle-concentration end-member behavior (granular flow type) is typically inferred from massive, unsorted, coarse-grained (m-size boulders) deposits, which are attributed to pyroclastic currents, where sediment transport is accomplished through a dense granular flow dominated by particle interactions (e.g. Lube et al. 2007, Bernard et al. 2014). The low particle-concentration end-member (turbulent flow type) is inferred from sediments organized as cross-laminated bedsets forming dune bedforms, that are generally finer and better sorted in terms of grain-size distribution (e.g. Walker 1984, Cole 1991, Douillet et al. 2013a, 2013b). The associated depositional areas organize as marginal and localized patches on the outer overbanks of pathways of the main pyroclastic current (e.g. Douillet et al. 2013a and references therein). For such deposits, the transport mechanisms are interpreted as being related to "fully-dilute" pyroclastic currents i.e. currents with relatively low particle concentrations and flow dynamics largely dominated by turbulence of the fluid phase (gas, e.g. Wohletz and Sheridan 1979, Branney and Kokelaar 2002, Dellino et al. 2004, Douillet et al. 2013b). Sedimentological analyses are however complicated by the fact that the deposits mostly reflect the influence of the flow-bed boundary layer rather than entire transport process (Branney and Kokelaar 2002, Douillet et al. 2018/2019). Furthermore, a continuous spectrum of deposit types is observed so that the boundary between these two end-members seems diffuse (Brown and Branney 2013 and references therein). These deposit-based models have been validated and refined through theoretical,

analogue and numerical models (Dufek and Bergantz 2007, Esposti-Ongaro et al. 2008, 2011, Sulpizio et al. 2014), which highlight the interplay and coupling between dense underflows and overriding turbulent currents (Burgisser and Bergantz 2002, Gladstone et al. 2004, Breard et al. 2016, Breard and Lube 2017).

Where transport is supposed turbulent (dilute pyroclastic currents), such flows are thought to resemble the characteristics of subaqueous turbidity currents (e.g. Gladstone et al. 2002, 2004). Indeed, in contrast with traditional aeolian and river sediment transport, dilute pyroclastic currents likely behave as particulate density currents (Kneller and Buckee 2000). Particulate density currents receive their momentum through their larger density compared to the ambient fluid. Their particularity is that the agent carrying this excess density is the transported particles. The same particles that drive momentum during transport thus also constitute the sediment that deposits when momentum decreases. The particles in a particulate density current are distributed over the whole height of the current rather than being eroded and transported near the bed only (e.g. Douillet et al. 2014). These subtleties make the dynamics of transport and deposition of particulate density currents unique, in particular when considering density stratification (Gladstone et al. 2002, Borwn and Branney 2013). Here, intriguing structures grouped under the term "shark-fins" are documented. They consist of a few overturned laminae over a decimeter scale extent, and occur as successive, periodic patterns on the lee side of dune bedforms.

1.2. Soft sediment deformation at the flow-bed boundary

Geological outcrops exhibiting convolutions or patterns associated with the deformation of sediment strata have been recognized for more than 150 years (Logan 1863, Allen 1982 pp. 343-393, Maltman 1994 and references therein). The processes of soft sediment deformation (SSD) are understood as the deformation of sediment beds before their consolidation (see review by Shanmugam 2017). They are generally interpreted to occur when a granular bed acquires a transient property of a liquid, either due to shaking -i.e. liquefaction- or due to an upward movement of the interstitial fluid -i.e. fluidization- (e.g. Lowe 1976, Nichols et al. 2010). Soft sediment deformation can occur either during the emplacement phase or as a post depositional process (e.g. Owen et al. 2011). In pyroclastic deposits, a variety of soft sediment deformation structures and triggers have been invoked, such as ballistic impacts, deformation by pressure waves produced by eruptive explosions, post depositional deflation of a fluidized flow, or basal shear from a granular-based flow (Douillet et al. 2015). When linked with the emplacement phase, soft sediment deformation structures can inform on the flow-bed boundary state during transport. Recent analogue experiments have shown that the velocity profile of a laminar flow can penetrate into a sediment bed on a short diffusion thickness, and thus a shear component is partitioned out of the flow (Houssais et al. 2015).

1.2.1. "Shark-fin structures"

"Shark-fin" is defined here as a generic term to refer to a particular type of soft sediment deformation structures resembling fins of sharks swimming upstream: the stratal organization indicates that the bed was superficially slightly translated downstream (Fig 1A). This results in a narrow overturned structure that is laterally confined. Here, shark-fins involve only a few laminae, and are often found periodic, "in-train" structures. The upper limit of these overturned beds is not planar, but rather forms a positive topographic anomaly. Several types of structures outside the pyroclastic context fall in the group of shark-fins and have variously been termed "imbricated flame structures and pseudonodules" (Larsen 1989), "flow oriented convolute beds", "flames" (Butler and Tavarnelli 2006), "truncated flame structures" (Matsumoto et al. 2008), or "asymmetric flame structures" (Butler et al. 2016). Shark-fin patterns have particularly been reproduced in the pioneering experiments of McKee et al. (1962a, 1962b) by "crinkling" laminated beds through different techniques: slumping, vertical loading, but also dragging sand bags across the surface or by artificially inducing strong currents at the bed interface. Here, shark-fins are described based on natural deposits from the 2006 pyroclastic currents at Tungurahua volcano (Ecuador). Shark-fins have been sparsely reported but rarely systematically investigated and it is speculated that they are common in many settings.

1.2.2. Overturned structures excluded from a classification as shark-fins

-"Sheath folds" share a similarity in shape with shark-fins in flow-parallel view (Carreras and Druguet 2018). The term sheath folds is not used here because although sometimes associated to purely clastic slumps (e.g. Strachan and Alsop 2006), it generally bears a connotation of ductile processes from diapirism, rheomorphism

or metamorphism (Branney et al. 2004, Alsop and Holdsworth 2006, Alsop et al. 2007). Shark-fins are defined exclusively as consisting of individually undeformed clasts. The equation set developed for shark fins (section 4) may however be transferable to some sheath fold structures.

-"Conventional overturned beds" (Fig 1B) is used here for patterns in sediment beds where (i) a stratal package contains a laterally coherent overturn of a large amount of laminae, (ii) this overturning occurs over a length much greater than the thickness of the deformation and (iii) the boundaries of the bedsets are planar and unaffected by the deformation. Thus, the localized extent of shark-fins is dissimilar to such conventional overturned beds (Fig 1). Whereas most authors agree that conventional overturned beds are formed in relation to a current, various processes have been suggested for the specific mechanisms, such as the pure shear of the flow, the scraping of logs and debris transported by a current, or a combined effect of earthquake-induced liquefaction while a current shears the bed (Allen and Banks 1972 and references therein).

1.3. Syn-flow shear structures in sediment flows

1.3.1. Basal shear inferred for pyroclastic currents

The influence of shearing by a pyroclastic current on its aggrading substrate was has been discussed in light of various sedimentary indicators. Crowe and Fisher (1973) were the first to note that "tightly folded overturned anticlines and synclines" "showed the evidence of the influence of the currents on their origin" at Ubehebe (California). Without explicitly mentioning overturned structures, Fisher (1990) recognized finger-like dikes of pyroclastic material intruded in the unconsolidated substrate at Mt St. Helens (Washington). He suggested that the flow head ploughed into the soil and mixed it, and that the structures may have been "caused by vortical motion, rotating material from within the head of the blast surge to the ground surface during erosion of the furrow". Cole et al. (1993) proposed that gradings of breccia/lithic concentrations at Roccamonfina (Italy) were related to "internal shear producing overriding or overlapping of the rear of the flow onto the slower-moving front part". On another Roccamonfina sequence, Gianetti and Luongo (1994) evidenced "flame structures stretched in the flow direction" on the crest of a duneform, and interpreted them as due to loading by subsequent flows. Reverse faults (ca. 30-60 cm-long) that offset the basal contact of an ignimbrite at Monte Cimino (Italy) were interpreted as syn-depositional substrate deformation due to the shear of the pyroclastic current (Laberge et al. 2006). Parejas et al. (2010) documented outcrops from Villarica (Chile) described as "folded, sheared, and thrust-faulted along the contact" that correspond to the definition of shark-fins -see their figure. 9-. They also noted that "subtle erosion and amalgamation surfaces [...] showed that the pulsatory flows were able to remobilize ignimbrite laid down earlier during the same eruptive phase". Meter-scale features from the Poris Ignimbrite (Tenerife) and some small-scale flame structures from the Tanjung Formation (Indonesia) were related to syn-flow shear instabilities by Rowley (2010). Douillet et al. (2015) documented small-scale shark-fin patterns in relatively massive units from the Ubehebe Crater (California) and additionally identified the signature of the migration of shark-fins in examples from the 2006 deposits of Tungurahua. Following Rowley et al. (2011), they interpreted these as structures that would result from the freezing of granular Kelvin-Helmholtz instabilities. From a theoretical analysis, Douillet et al. (2015) suggested that such instabilities would develop for relatively slow-moving mixtures (generally below 0.5 m/s). Recently, Brand et al. (2017, figure 10) recognized large-scale patterns similar to shark-fins in the deposits of the 1980 pyroclastic currents of Mt. St. Helens (Washington). They seem to have occurred when the main flow interacted with localized lenses of material from a previous flow.

1.3.2. Shear structures from sediment flows

In a broader context, numerous studies have addressed the question of how density and granular currents interact with the erodible substrate upon which they flow. Several experiments have shown that granular flows are prone to develop wavy patterns and shear instabilities at the flow-bed boundary with a granular bed (Goldfarb et al. 2002, Rowley et al. 2011, Verhagen et al. 2013, Roche et al. 2013, Farin et al. 2014). A variety of overturning and vortical structures can also form within a granular flow, including longitudinal vortices (Forterre and Pouliquen, 2001), shear breaking waves (Goldfarb et al. 2002), Tailor vortices (Conway et al. 2004) or recirculation loops (Caicedo-Carvajal et al. 2006). In deposits of turbidity currents (in the broad sense of subaqueous particulate density currents), a variety of structures have been attributed to flow shearing and deformation during the emplacement phase (e.g. Dzulynski Smith 1963, Larsen 1986, Butler and Tavarnelli 2006 Postma et al. 2009, 2014, McClelland et al. 2011, Eggenhuisen et al. 2011, Marques 2012, Butler et al. 2016, Gladstone et al. 2017).

Under the assumption that a flow is a closed system that primarily interacts and exchanges energy between its basal part and the bed (and to some extent, at the upper free boundary with the ambient fluid), syn-depositional overturned patterns can yield valuable information on the dynamics and rheological parameters of the parental currents. Here, shark-fins are investigated from a dataset of >220 natural structures, including measurements, discussion of their origin in terms of physical processes, and the application of an equation framework for quantitative analysis.

2. DATA

2.1. A dataset based on the 2006 eruption of Tungurahua

The structures reported here are preserved in the deposits from the 17 August 2006 eruption of Tungurahua volcano (Ecuador). This eruption triggered the formation of pyroclastic currents that were funneled in ravines of the fluvial drainage network on the steep flanks of the volcano (e.g. Kelfoun et al. 2009, Douillet et al. 2013a, 2013b, Bernard et al. 2014, Rader et al. 2015, Benage et al. 2014, 2016). Cross-laminated sediments forming dune bedforms dominated by ash are preserved as marginal, isolated patches with an extent of several hundreds of meters on the overbanks of the ravines that directed the flows (Douillet et al. 2013a, 2013b, 2019). For this study, several bedforms were cut open in longitudinal transects in the field and impregnated with an epoxy resin in order to produce sediment plates -a type of lacquer peels (Douillet et al. 2018, 2019). Such sediment plates capture the natural lamination patterns at a highly detailed resolution (Douillet et al. 2019), which enabled to observe the overbent flames and convolute laminae grouped under the term shark-fins. All shark-fin structures documented here were observed in these cross-laminated dune bedforms and co-exist within bedsets including (Fig 2, Douillet et al. 2013b, 2019):

- (i) a general stoss-depositional tendency,
- (ii) horizontal to sub-vertical truncations of stoss-faces,
- (iii) planar laminasets evolving into stoss-aggrading ripples,
- (iv) a partial to total absence of stratification (diffuse to massive aspect) in some beds, laterally evolving into diffusely laminated beds, and
- (v) a dominance of planar lamination on the lee of crests.

It is worth emphasizing at this stage that no liquid water was involved in the flow of the pyroclastic currents and that intact leaves and wood fragments found in the deposits testify to a low emplacement temperature (no welding or rheomorphic flow).

A set of four sediment plates from four different bedforms and two sets of four parallel sediment plates from two other bedforms were screened (Fig 2). They represent the entire range of shape types identified in Douillet et al. (2013b). Each sediment plate has a length of 3 m aligned with the flow direction, and heights varying between 0.8 and 1.8 m, thus representing ca. 43 m^2 of outcrop. Deformation patterns were absent in two dominantly massive and coarse-grained bedforms (lapilli / gravel sizes dominated), but present in all fine-grained outcrops (ash / sand size range).

2.2. Description and classification:

The shark-fin patterns form an overturning of laminae and are elongated toward the down-flow direction exclusively. They consist of a "tail" which is linked to the laterally adjacent planar laminae via "roots" (Fig 1A). In total, 223 structures were identified, described, measured, and classified (Fig 2). Three different end-members were recognized based on their cross-cutting relations (Fig 3):

- "*convolute shark-fins*" (146 structures, Fig 3A, 4): the overturned tail can be followed laterally to non-deformed sets without a truncation of the lamination, so that the tail is connected to the two roots upflow and downflow. The laminae are fully preserved.
- "*truncated ripple shark-fins*" (64 structures, Fig 3B, 5A-D): the patterns are found at the limit of a ripple-sized heap delimited by a truncation of the laminae. The tail is truncated and overturning is visible from the limit of the roots.
- "*flat truncation shark-fins*" (13 structures, Fig 3C, 5E): truncated overturned laminae are found underlying a flat and laterally continuous erosion plane over a limited length (< 10 cm).

A variety of overturned geometries is recognized, spanning the range between smoothly distributed overturning forming bulbous, rounded style tails (e.g. Fig 4B) to highly angular tails bent only at localized knickpoints giving a "chevron-like shape" (e.g. Fig 4A, 4D). Note as well that almost no documented features have their tail dipping downward (aligned with the gravity force), and the patterns are only elongated in the downflow direction without vertical re-arrangement. The shark-fin patterns are wholly dissimilar to "conventional overturned beds", which include an entire stratal package on a much broader lateral extent (e.g. Allen and Banks 1972, see 1.2.1). A classification as tectonic/metamorphic "sheath-fold" is also excluded. Indeed, the 2006 deposits containing shark-fins are emplaced at the surface, have never been buried, and consist exclusively of undeformed particles deposited at low temperature.

2.3. Occurrence and spatial recurrence:

2.3.1. Occurrence

Most shark-fin structures occur on the lee side of bedforms, on a flat or gently dipping palaeo-surface (lamina or erosion) with slope between -5º (i.e. reverse) and 25º (Fig 2, 10). Shark-fin structures are most common in three types of settings (classified in Table in Annex):

- in relation with a low-angle erosion plane (Fig 6A),
- within a zone of disturbed beds (occurring as confined lens or continuous layer) concordant with the dip angle of the lee side of a dune bedform (Fig 6C, 7-8),
- downstream from a surface irregularity at the respective horizon. These irregularities can take the form of a small scour or gulley (Fig 7C), the crest knick-point of a metric dune form (Fig 7D), or an accidental small block lying on the bed surface.

2.3.2. Spatial recurrence

Shark-fin structures are often organized as pairs, triplets or quadruplets and rarely more, and a single train can be formed by different types of shark-fins together. The spacing between these groups is generally small (5-50 cm), and the patchy organization can be expressed in two ways:

(i) along a single horizon with downstream repetitions (i.e. “wavy in-train patterns” concurrent in the same temporal interval, Fig 6A, 7).

(ii) "amalgamated" at different stratigraphic levels, yet at close location and generally within the same co-sets (i.e. climbing in the stratigraphy - spatial stability in time, Fig 6B, 8A-B).

Where they occur “in-train” on the same horizon, the length between successive “shark-fins” was systematically measured (Fig 9A, Table in Annex). Whereas the inter-structure distances are *a priori* not correlated, they appear to be arranged as multiples of each others within a single train. Fairly periodic patterns become evident upon dividing the separation length by 2 or 3 (which corresponds to plotting the harmonics in the case of a wave, Fig 9B). This suggests that an actual wavelength is present, yet not always apparent as some of the shark-fin occurrences are not visible in the deposits.

2.3.3. Ploughed zones

Many of the shark-fins are laterally accompanied by zones that seem substantially disturbed, where lamination is only diffuse and lineations oblique to the bedsets are visible (Fig 6C, 7C-D, 8B-C). These zones seem to have undergone consequent mixing, and their grain size distribution is less sorted than that in non-disturbed beds. Here, the term "ploughed zones" is used in the description to refer to these thin lenses accompanying shark-fin trains (Table in Annexe).

2.4. Dimensions

For each shark-fin, a series of parameters were measured (Fig 1A, 10, Table Annex 1): length (the extent of the deformed zone), thickness (from root to top of tail), elongation (the length of overturning), number of overturned laminae, grain-size and stratal organization of underlying and overlying beds, slope angle of affected beds and affecting contact, lateral continuity (up- and downstream), distance to the next structure when part of a train, and position within the outcrop (Fig 2, 9-10).

At Tungurahua, the dimensions of the shark-fins are relatively homogenous (Fig 10), and vary by only one order of magnitude, both in terms of length, thickness, and number of affected laminae (Mean/Max/Min values

of 5.68 / 20 / 1.5 cm for length, 1.48 / 5 / 0.3 cm for thickness and 9.19 / 24 / 3 for affected laminae, respectively). Although linear regressions were plotted to highlight trends in the graphs, we do not conclude linear trends for these structures, and the data are quite broadly distributed within the entire dimensional windows (Fig 10). The thickness of deformation remain superficial and never exceed 5 cm. The subgroups of convolute- / truncated-ripple- / flat-truncation- shark-fins differ in trends mainly because convolute shark-fins tend to be thicker for similar lengths/number of involved laminae/elongation. This might be expected as a truncated structure is likely to be less thick than a fully preserved one.

2.5. Overturned patterns not satisfying the shark-fin criteria

Three zones had particular overturned patterns that do not belong to a shark-fin classification (Fig 11, 12) but are reported hereafter and interpreted separately (see Discussion, section 5.2).

2.5.1. Abnormal disturbed zones

One transect of the lunate bedform (Fig 11A) exhibits atypical overturned structures with a bulbous shape (Fig 11C-E). These occur in zones including unconformities and deformed patterns deviating from the usual trend (pink zones in Fig 11A). These zones are initiated directly downstream a paleo-crest on the lee side (Fig 11B). There, enigmatic step-like "crinkled" laminae are underlined by a scar forming a basal unconformity that gradually becomes conformable downstream. They contain an association of 1) bulbous overturned structures either laterally in-train or vertically spread, 2) intact planar lamination, 3) massive zones, 4) diffuse laminasets possibly representing ploughed lenses. These abnormal zones are ca. 15 cm-thick, and can be followed over a length of >2 m. Three of these onset-scars are clearly recognized, and their accompanying disturbed zones vanish or become mixed together farther downslope (Fig 11A).

The beds above these abnormal zones are diffusely stratified to massive, appear to be reworked or disturbed in places, and exhibit sets of "backset lineations" with very steep angles that are organized in lenses ca.1 cm-thick and 15 to 20 cm-long (Fig 11D). The nature of these "lineations" is unclear, and could either be attributed to constructive laminae, to the underlining of regressive truncations, or they could represent a reworked facies.

2.5.2. Sediment-dike

In the transect from an "elongate bedform", a coarse-grained and massive layer splits into two separate layers (Figure 12). On the upper stoss face of the bedform, the layer (ca. 9 cm-thick) locally branches out into a 15 cm-long basal "sediment-dike" (ca. 3 cm-thick) and overriding upper layer (ca. 6 cm-thick). In-between the split layers, a laminaset of fine-grained sediments is sandwiched and deformed in chevron-like patterns (Fig 12). The basal part of the sediment-dike shows a "pickled" surface that intrudes into the underlying contact. Directly downstream from the branching, a slip surface emanates from the base of the split layer and displays a short throw in the downstream and upward direction with an angle of ca. 15º, with overturned layers underlying the fault trace. Around 60 cm further downstream, a coarse-grained lens resembling the basal layer appears in the section and may be a prolongation of this basal bed.

2.5.3. Steep overturning truncations

Very steep truncations are visible on the stoss sides of bedforms and can reach dip angles above 80º. Some of these truncations are underlined by a cm-scale zone where truncated laminae are coherently overturned over distances of up to tens of cms (e.g. figure 5D in Douillet et al. 2019). Such structures are referred to as "steep overturning truncations". They are reported in the location maps of the shark-fin structures, since shark-fin patterns may develop in-train with the crests of "steep overturning truncations", but not discussed here (see e.g. Douillet et al. 2017).

3. INTERPRETATION

The interpretation is based on the common shark-fin patterns observed in the deposits as well as existing evidences from the literature. Altogether, this information point toward stable waves that develop on a shear horizon at the flow-bed boundary as the physical explanation for the formation of shark-fins (this section). The inference of this process then enables the use of a physical model in order to further constrain the stability of the structures (section 4). The irregular overturned patterns (section 2.5) are treated separately in the discussion, as the observations suggest different triggers (section 5). Such processes may form structures resembling shark-fins but result from completely different dynamics.

3.1. Existing literature

3.1.1. Wavy shear patterns at the flow-bed boundary of experimental sediment flows

The question of how granular flows interact with the erodible substrate upon which they flow has been studied in various contexts. Recent analogue experiments have demonstrated that local wavy patterns and shear instabilities can develop at the interface between a flow and its substrate. These phenomena can have crucial effects on the dynamics and rheological parameters of a flow. Vortex instabilities are well known from granular gas and granular flow theories (e.g. Mitrano et al. 2012).

A fundamental study on wave instabilities in a granular medium was carried out by Goldfarb et al. (2002), who reported that “breaking waves” (i.e. vortical, repetitive in-train wave instabilities) could form at the vertical interface between two streams of identical grains. They suggested that the competing shear and extensional strains produced such instabilities. Rowley et al. (2011) produced vortical patterns preserved in deposits where a decelerating granular flow passes over a stratified substrate of similar grains. These structures have been observed on vertical transects, and thus a gravitational component in the force balance was present. The vortical shapes may also suggest a rotational component linked to buoyancy. The vortices occurred in trains of several repetitions, suggesting their formation through an oscillatory (wave) mechanism. Although pointing out the differences inherent in the physics of granular flows, Rowley et al. (2011) compared these patterns with Kelvin-Helmholtz instabilities occurring in fluids.

For the case of subaqueous environments, Verhagen et al. (2013) launched a series of studies on the interaction of sediment gravity flows with their substrate. They released clay-laden, bottom-hugging density currents over a loosely packed, “fluidized” bed of clay, and showed that these could interact and form “interfacial waves” at the flow-bed boundary, “leading waves” ahead of the front of the current, or induce "chaotic mixing" with the substrate. They noted a dependency on the stability field of each type of interaction with the dimensionless Richardson number, without explicitly mentioning gravity waves or Kelvin-Helmholtz instabilities. In a similar setting focused on subaerial lock-exchange granular flows, Roche et al. (2013) showed that “the sliding head of a granular flow generates a dynamic upward pore-pressure gradient at the flow-substrate interface. The associated upward air flux was enough to fluidize a substrate of fines, so that particles were not entrained individually but the substrate instead [was] subject[ed] to small shear instabilities”. Using the same setup, Farin et al. (2014) refined the observation, noting that granular flows formed “waves made of particles excavated from the erodible bed at the flow head” and that their maximum amplitude increased with the aspect ratio and volume of the released flow. They also compared these waves with Kelvin-Helmholtz instabilities. Recently, Pollock et al. (2017) experimentally triggered the growth of in-train, repetitive wave-like features along the interface between a high pore-pressure granular flow in a frictional regime. These authors were able to vary the scale of the features as a function of the fluidization state.

3.1.2. Shear structures and overturned beds in natural turbidites

A variety of shear structures have been attributed to flow shearing in deposits of turbidity currents (in the broad sense of subaqueous particulate density currents). Early workers noted for deformed turbidite beds that "convolutions are a fossil record of the forces which operated upon laminated bed during its sedimentation" (Dzulynski Smith 1963). Larsen (1986) interpreted that "oblique flames and pseudo-nodules" resulted from shearing of loosely packed deposits caused by the still moving turbidity currents. Butler and Tavarnelli (2006) postulated a deformation during the emplacement phase from the interpretation of a combination of flow-aligned mud injections, boudinage and sheared flames. Postma et al. (2009, 2014) identified flame structures elongated/overturned in the paleoflow direction at the border of steeply truncated beds. They compared these structures to footages of a series of analogue experiments on Froude-jumps within turbidity currents, where reworking of the bed was triggered by variations in the intensity of a Froude-jump in its "pool". "Substrate wings" from detachment, convolute laminations, sills and dikes were documented at the base of turbidite beds and linked with erosion steps from these flows (Eggenhuisen et al. 2011). Eye and sheath folds, occurring in intervals of 2-10 cm thickness together with convolute laminations have tentatively been related to the syn-depositional shear strain from turbidity currents acting on an aggrading ripple bed substrate (McClelland et al. 2011, Marques 2012). Several classification schemes and criteria have been proposed to figure out the exact timing and processes of syn-depositional shearing generally invoking a density-driven Kelvin-Helmholtz mechanism (Butler et al. 2016, Gladstone et al. 2017).

3.2. General flow conditions

3.2.1. Turbulent flows

The fields of dune bedforms produced by the 2006 eruption of Tungurahua have been interpreted as deposited from diluted pyroclastic currents (Douillet et al. 2013a, 2013b). The mm-thickness of laminae most likely resulted from fluctuating and pulsating conditions in the current affecting sedimentation, and turbulence remains the best potential explanation for these laminations. The inference of turbulence points toward a parent flow dominated by the dynamics of the fluid phase rather than by particle interactions. This further implies a rather low particle-concentration, falling in the field of "traction-dominated flow boundary zone" of Branney and Kokelaar (2002).

3.2.2. Syn-depositional shearing

Since many of the shark-fins are truncated and covered by planar laminae, overturning likely occurs briefly after deposition and before or during sedimentation of the directly overlying beds, and is thus taken as a syn-flow process. As already pointed by Allen and Banks (1972) for conventional overturned beds, the unidirectional alignment with the downflow/main-slope direction suggests a mechanism driven by the transport of the flow. Our interpretation is that the basal shearing of the flow is the cause.

Given that a single train of shark-fins can include a mix in any order of "convolute", "truncated ripple" or "flat truncation" structures, these three types should result from a similar process. Consequently, truncated shark-fins likely represent a cut version of convolute ones, an assumption supported by the fact that truncated structures follow the same dimensional trends as convolute ones, but are thinner (Fig 10).

3.2.3. Traction carpets / granular boundary layer

The general laminated nature of the deposits points toward parental turbulent and dilute currents. However, the formation of shark-fins specifically is unlikely to result solely from low-concentration flows in fallout or saltation only. Indeed, in order to preserve the coherence of the lamination during the formation of shark-fins, the deformation must occur as packages (e.g. Roche et al. 2013). Accordingly, saltation, where particles are moved individually is not an adequate process (e.g. Douillet et al. 2014). In contrast, maintenance of coherence requires a flow which was sufficiently concentrated and which yielded sufficient strengths to deform the underlying bed. Thus it is suggested that thin granular flows, likely basal traction carpets (see Sohn 1997), interacted with the bed boundary in the form of superficial granular shear. Such a granular base is further supported by the fact that most experimental observations of shear structures were made from granular flows (Goldfarb et al. 2002, Rowley et al. 2011, Roche et al. 2013, Farin et al. 2014). As such, the pyroclastic currents creating the shark-fins horizons can be envisioned as thick turbulent flows, but with a thin granular base that is fed by the particles falling from the turbulent part, in agreement with observations elsewhere (eg. Brown and Branney 2013, and references therein).

3.3. A wave interface at a shear horizon

3.3.1. Periodic patterns (waves)

The repetitive nature, on the same horizon (in-train structures), together with the occurrence of a pseudo-wavelength (modulo harmonics) suggest that the process forming shark-fins behaves as a wave, i.e. an oscillatory mechanism with a spatial periodicity. It follows that the numerous signs of disturbance directly upstream of shark-fins, or along a horizon containing shark-fins can be interpreted as the mark of shark-fins migrating laterally. These signs would thus represent the lateral displacement of the parent waves. At Villarica, Parejas et al. (2010) already noted "subtle erosion and amalgamation surfaces", possibly related to the same processes. This supports the reasoning of Rowley (2010) for the rare occurrence of shark-fins: "The structures [might] exist but migrate laterally through a steady current, leaving no recognizable feature other than a well-mixed zone in their wake".

3.3.2. Timescale of growth vs. sedimentation

Shark-fins can be found amalgamated in clusters that translate on nearby lateral positions in successive laminae, i.e. with a vertical jump of shark-fins in stratigraphy. This observation has two consequences: 1) a relative spatio-temporal stability during aggradation may be inferred. 2) Importantly, if shark-fins develop

over several laminae, their growth must have a temporal scale that is similar to the aggradation rate. More generally, for shark-fin patterns to be preserved in the deposits, these should grow rapidly enough to produce the characteristic overturning before the interface is buried. Rowley (2010) speculated that the infrequent occurrence of shark-fins might be related to such a timescale equilibrium: "[Pyroclastic current] flow boundary zones [might] migrate vertically too rapidly for K-H-like instability [i.e. shark-fins] growth to occur". On the other hand, if the shear instabilities grow too fast, they may completely mix the existing stratal organization and rework any interface into a completely ploughed or massive layer, and thus no shark-fins could be observed (as also speculated by Rowley 2010). Here, it is thus interpreted that the growth rate of the wave instabilities forming shark-fins are comparable with the aggradation rate of the sediment bed during emplacement.

3.3.3. A mechanism at the boundary layer triggered by the bed shape

Shark-fins are often concentrated directly behind a crest or a local break in slope of the paleo-topography, with several occurrences dispatched over successive lamina (depochron). Similarly, Kuenen (1953) described folded beds associated with ripple beds (possibly due to pressure drops on the lee of the bedforms) whereas in the context of sheath folds, Cobbold and Quinquis (1980) noted that "passive folds can develop by kinematic amplification of deflections". All together, these information show that irregularities of the bed configuration are prone to trigger the formation of the wavy shear interfaces. This further points that shark-fins originate from a nearbed instability at the flow-bed boundary layer rather than from the upper parts of the flow.

3.3.4. 'Holmboe' instead of 'Kelvin-Helmholtz' instabilities

Several authors have related shark-fin patterns to granular Kelvin-Helmholtz instabilities (Rowley et al. 2011, Farin et al. 2014, Douillet et al. 2015, Gladstone et al. 2017) or showed through relationships of the Richardson number (ratio of buoyancy over shear forces) that density stratification is involved (Verhagen et al. 2013). In fluids, a range of shear instabilities have been observed and modeled, in particular, Kelvin-Helmholtz and Holmboe instabilities (e.g. Lawrence et al. 2013). In a stratified fluid flow, Holmboe instabilities supplant Kelvin-Helmholtz instabilities when the density gradients are more abrupt than the vertical changes in flow velocity (e.g. Smyth and Winters, 2003). Both Kelvin-Helmholtz and Holmboe phenomena could produce patterns similar to shark-fins if transposable to the granular context.

In terms of shapes, shark-fins are quite dissimilar to Kelvin-Helmholtz instabilities, which develop typical vortex structures. Instead, the shark-fins strikingly resemble the Holmboe patterns observed for fluids (e.g. Lawrence et al. 2013). Furthermore, the Kelvin-Helmholtz instability produces a vortex *at* the interface whereas the Holmboe problem results in a pair of standing waves focused *around* the shear zone and includes the idea of a thickness of deformation, as observed for shark-fins (Menczel and Kostaschuk 2013).

The basic theoretical frameworks for Kelvin-Helmholtz and Holmboe instabilities in fluids differ essentially in the nature of the velocity and density interface between the two sheared fluids, resulting in different stability fields and growth rates. Strictly speaking, Kelvin-Helmholtz conditions consist of two sheared fluids with a sharp velocity and density interface, whereas the Holmboe case assumes a linear velocity gradient around the density interface (see e.g. Lawrence et al. 2013). The Holmboe configuration thus appears more suitable to the shark-fin case with a transitional boundary between a granular flow and granular bed. Furthermore, for a granular flow on a granular bed, a low density contrast but strong velocity gradient is expected, a situation where Holmboe instabilities would supplant Kelvin-Helmholtz ones (see Smyth and Winters, 2003 for details).

Whereas it seems probable that the granular flow at the origin of the shear is less concentrated than the bed, the influence of the restoring gravity force is unclear. Sedimentological evidences could include a downward bending of the tail of shark-fins (due to their excess weight compared to the overlying shearing fluid), but this was not observed. The grain size distribution of both affected and overlying beds are variable, and no rules concerning a possible bed density inversion was observed, in contrast to the suggestion in other deposits (Gladstone et al. 2017). A Holmboe instability thus appears again more probable than Kelvin-Helmholtz. Notably, the granular experiments of Goldfarb et al. (2002) produced vortical, repetitive in-train wave instabilities at a vertical interface, therefore not involving density but rather the competing shear and extensional strains as destabilizing and restoring forces.

Alternative interpretations to the Kelvin-Helmholtz/Holmboe instabilities could include several periodic phenomena that shear a bed, e.g. Taylor vortices (e.g. Conway et al. 2004), stress chains within a granular bed that periodically "touch" the bed (e.g. Taboada et al. 2005), or the saltation of a larger clast that produces an overturning at each bouncing location (e.g. figure 4 in Douillet et al. 2015). In the absence of any solid recognition criteria, these alternatives are only evoked but not further discussed and developed.

4. THEORETICAL FRAMEWORK

4.1. Model

A theoretical equation framework is presented in order to translate the observation of the natural deposits (periodicity, thickness of deformation zone) into quantitative estimates of parental flow parameters (Fig 13A, Annex 2). Similarly to Kelvin-Helmholtz or Holmboe instabilities, the model seeks to resolve the Taylor-Goldstein equation. Although based on the Kelvin-Helmholtz and Holmboe problems, the initial conditions differ slightly in order to include most of the interpretative conclusions (Fig 13B):

1) A flow with constant velocity "U" represents the basal granular traction carpet and flows horizontally on the bed. The upper turbulent part of the flow can be neglected and the flow disturbance is considered as confined within this viscous sublayer in which the velocity profile is linear. Indeed, the problem can be solved by neglecting the turbulent fluctuations (Reynolds turbulent stresses) if:

$k^* \delta_v \geq \square 10{-}2$ *with* $k = 2 * \pi / \lambda$ *and* $\delta_v = \nu / u_*$ (Charru et al. 2013).

Using an average value of $\lambda = 0.15\ m$ (Fig XX), $\nu = 15\ 10^{-6}\ m^2\ s^{-1}$ (the viscosity of air) and $u_* = 0.1\ m\ s^{-1}$ (measured from wind tunnel experiments with pyroclasts, Douillet et al. 2014), $k^* \delta v = 0.63\ 10^{-2}$, in the order of the approximation limit. Note that the viscosity of an air-particle mixture is likely higher than for pure air, so that this estimation is likely underestimated.

2) The flow is separated from the bed by a horizontal shear layer of thickness "$2*d$" that represents the zone of shark-fin formation. This shear layer has a linear (laminar) velocity gradient with height, representing the effect of viscosity, as for the Holmboe problem. However, unlike the Holmboe case that has a sharp density gradient, density is taken to be constant in the shear zone, since this is envisioned as a mixing zone.

3) The initially horizontal upper and lower interfaces of the shear horizon are perturbed with a coupled wave of low amplitude ("η" with wavelength "λ") that corresponds to the periodicity observed in shark-fin recurrence. Both perturbations can be taken as coupled and in phase. Indeed, for small wave slopes and in the case of a linear stability problem, the disturbance of a flow is a linear response to the bed profile and is almost in-phase (see e.g. figure 2 in Charru et al. 2013).

4) The analysis tackles the stability of these wavy interfaces and consists in quantifying the growth rate of the early forming waves. For preservation of the frozen instabilities in the sediment, the growth rate is thought to scale the sedimentation rate.

5) No insight is available to prove any influence of gravity as a restoring force. Yet, this remains a likely parameter. Thus, two sets of equations are developed, which differ only in their initial configurations: one considers a constant density for the three layers of the problem (similar to the Rayleigh problem), whereas the other case considers a linear vertical density profile for the upper and lower media.

The model (fully developed in Annex 2) is based on a relatively well-known configuration (see e.g. Sutherland 2005). For simplification purposes, the flow and the bed are considered as two incompressible, semi-infinite (unbounded), and unidirectional flows in the horizontal axis. The momentum and continuity equations are solved for small perturbations that are finite and propagating in the vicinity of the shear layer only. Considering the assumption of incompressibility, density can be advected but not diffused. Resolution enables to use the Rayleigh/Tailor-Goldstein equations for piecewise linear profiles of velocity and density. In complement to the basic Kelvin-Helmholtz equation set (e.g. Drazin 2002, p.45-47 or the Annex of Douillet et al. 2015), this model accounts for a layer containing a viscous shearing that acclimates the deformation and implicitly contains viscous dissipation forces.

4.2. Linear approximation

The dispersion equations ruling the growth rate of the waves were solved numerically (Fig 14A-B). Three variables intervene in the equation: (i) the wavelength "λ" -corresponding to the spacing between shark-fins, (ii) the thickness of the shear horizon "$2*d$", approximated through the observed thickness of shark-fins, and (iii) the flow velocity "U_0". The output is a colormap of the growth rate of the waves, i.e. the rate of increase in the waves' amplitude (Fig 14A-B).

The calculated growth rates are valid only until non-linear effects become non-negligible, a situation usually bound to the initiation of the perturbation. In a similar problem of ripple beds forming through the interaction with a viscous sub-layer, Charru et al. (2013, section 2.3) considered a linear response valid for $k * \eta \simeq 0.1$. Translated for the natural observations, this criteria becomes:

$$\lambda / H \simeq 62.8$$

Depending on the shark-fins, the criteria varies from "attained" to "10 times too small" (less than an order of magnitude, Fig 14C). The linear response is thus not strictly valid, but an approximation only.

The model with a density gradient is posed with the Richardson number ("*Ri*") as a variable, i.e. the ratio of restoring density force and perturbing shear force, which is defined as:

$Ri = N_0^2 * d^2 / U_0^2$; where N_0 is the Brunt–Väisälä frequency:

$$N_0^2 = (g / \rho_{mean}) * \partial\rho/\partial z$$

Considering a linear density profile in the sublayers, N_0^2 simplifies as $N_0^2 = g / d$, and the results for a density gradient can be plotted as a function of the flow velocity (Fig 14B). Interestingly, the main parameter of the problem thus concretely reduces to a length scale, a result already emphasized for buckling instabilities between two fluids that produced patterns similar to shark fins (Benjamin and Mullin 1988).

4.3. Model results and validation

Since the posing of the problem solely involves λ and d as length quantities, the dimensionless ratio of λ/d (hereafter, dimensionless wavelength) determines the growth of the wave interface (Fig 14A-B). The dependency on flow velocity (U_0) is very low, and patterns are stretched on a vertical axis.

In the "constant-density model" (Fig 14A), a sharp contrast between absence and extreme growth of waves is found for a dimensionless wavelength around 9, irrespectively of a flow velocity. In complement, another sharp contrast is found for very low velocities, irrespective of the dimensionless wavelength.

The "density-gradient model" results in much more stable waves because of the restoring effects of density, and the growth rates are better constrained (Fig 14B). Furthermore, the data of shark-fins observations of the recurrence length versus thickness of deformation -thought to represent a proxy of wavelength and shear layer thickness (Fig 14C)- are in good agreement with the "density-gradient model" (Fig 14B), i.e. the data plot within the zones of largest growth rates. In contrast, the field data are fairly out of the "constant-density model", thus invalidating this model, and the following analysis thus focuses on the "density-gradient model" only.

When plotted as a function of the Richardson number (Fig 15), the growth rate contours appear comparable with other similar analyses of stability and closely resemble the growth rates of Holmboe instabilities (e.g. Sutherland 2005, Lawrence et al. 2013). Interestingly, the contours of the growth rates are developed in a zone of higher dimensionless wavelength ratios and higher Ri than for Kelvin-Helmholtz instabilities (Fig 15 - inset, see Lawrence et al. 2013). These contours appear to better explain the observed dimensions of shark-fins here. The range of Richardson values corresponding to the highest growth rates would entrain laminar conditions, as was speculated in the initial conditions. The results of the theoretical framework thus suggest that the formation of shark-fins from wave instabilities in a configuration close to-Holmboe instabilities is feasible, and in good agreement with the field observations with a linear density gradient (Fig 13, 14B-C).

4.4. Preservation of shark-fins: pulsating sedimentation rate

In a typical problem, the instabilities are generally dominated by waves with the fastest growth rate (most unstable modes, e.g. Sutherland 2005). The field data are in good agreement with this scenario (Fig 14B vs. 14C). Additionally, the preservation of frozen shark-fins in the sediment through their burial is fundamental. Consequently, the approach here is to use the growth rates to infer plausible sedimentation rates for dilute pyroclastic currents in the deposition phase. Indeed, if the sedimentation rate is much higher than the growth rate, then no structures would have time to form whereas if the growth rate overrides significantly the sedimentation rate, then the structures are likely to completely mix the interface before they become frozen

(buried, see 3.3.b). Thus the peak of occurrence of shark-fins (Fig 14C) would suggest growth rates and consequently sedimentation rates varying from 0.4 to 0.1 m/s for a 5 cm-thick shear layer (median range of the observation). Few direct comparisons exist to validate this estimation. In their large scale pyroclastic current experiments, Breard et al. (2016) reported aggradation rates of 3.5 mm/s for crudely laminated layers but rates as fast as 450–550 mm/s for their main unit. The broad interval values of 0.01 to 0.4 m/s suggested here are thus comparable and considered as realistic sedimentation rates for the stratified deposits in which they occur.

Such high sedimentation rates strengthen the postulated occurrence of local traction carpets. Note that these high sedimentation rates are understood as almost instantaneous values. They are not meant to be extrapolated for a whole sedimentary unit, do not suggest an *en-masse* freezing and are compatible with a progressive aggradation scenario (Branney and Kokelaar 1992, 2002). Such sedimentation rates likely apply for individual lamina or laminasets, suggesting a form of pulsating sedimentation in a manner of the stepwise aggradation model of Sulpizio et al. (2007).

5. DISCUSSION

5.1. Overturned patterns unrelated to shark-fins

The irregular patterns documented here show forms of overturning that do not correspond to shark-fins. They suggest other types of imposed shear force, and remind us that extreme caution is indispensable when relating sedimentary structures to parental flow processes.

5.1.1. Slumping

The lunate bedform outcrop (Fig 11) provides strong arguments for slumping as a mechanism of deformation (Fig 16A). Indeed, the deformed zones are situated on steep lee sides (>20º) prone to gravitational destabilization. Their lateral continuity over 2.5 m and consequent thickness (>15 cm) suggest a larger scale process than the wave instabilities envisaged for shark-fins, and the unconformities forming the basal scars appear better explained by a fault than by an erosive event. The disturbed zones are relatively massive or disturbed, as if the material were mixed by a mass movement. The step-like "crinkled" forms at the onset of disturbed zones seem to be related to extension (Fig 11B), whereas the downstream ends contain deformation structures linked with a shortening (Fig 11C). This further suggests a downward movement of the disturbed lenses as a whole. Thus, brief destabilizations and short slumps on the lee side of the bedform are envisaged to explain these associations of overturned and disturbed patterns. Slumping, collapse or dynamic liquefaction has been involved in many previous interpretations for aeolian deposits - which share, with pyroclastic currents, the property of having air as the interclast fluid - (Allen and Banks 1972 and references therein, Chan et al. 2014, Ford et al. 2016). Horowitz (1982) invoked “an unequally distributed surface load created by sand dune topography“ to explain the deformed layers in aeolian dune foresets. Here, the cause of swaying could be a combination of the frontal (stoss) push of the pyroclastic currents, the rapid loading from the depositing mass, and oversteepening of the bedform (Fig 16A). The structure as a whole further testifies the metastable, uncompacted state of the sediment bed briefly after deposition.

5.1.2. Sediment-dike

The sediment-dike found in the outcrop from the elongate bedform has a singular configuration (Fig 12). It shows that the basal part of the flow locally penetrated at the base of the finer-grained sandwiched layer to form a small-scale injectite, whereas the top of the flow kept overriding the whole (Fig 16B-C). Similar "finger dikes" have been reported by Fisher (1990). Through analogue experiments, Baas et al. (2014, 2016) evidenced that “the lower part of turbidity currents has the ability to enter fluid mud substrates“. They were able to produce a mixing-zone around injectites, nodules at the interface, and sandwiching of the penetrated layer, as observed here. They conclude that such “intrabed currents are driven by bed shear stress exceeding the bed cohesive strength, and by flow density exceeding bed density“. The accommodation of a shortening in the sandwiched layer is testified by the chevron-like deformed laminae as well as the small thrust fault farther downslope (Fig 12B, 16C). The sandwiched bed was thus being squeezed. Besides the difference in densities and timescales, this squeezing share similarities with the "bulldozer effect" evidenced for rock glaciers (Morgenthaler and Frehner 2017). In that case, the bed is folded and forms a bulge at the front of a creeping rock-glacier. It is unclear whether the sandwiched laminaset was part of a continuous layer that was otherwise eroded away, or was a local lens deposited in the "pool" formed by the stoss of the bedform. The intruding material is coarser-grained, and could have been denser than the fine-grained sandwiched material at time of

(de)formation. Low cohesive strength of the deformed bedsets is expected for an intraflow to occur. Again, this suggests an unstable state of the sediment briefly after deposition, possibly partially fluidized.

5.2. Questions surrounding the occurrence of shark-fins

The origin of shark-fins from a combination of waves around a shear horizon triggered by a traction carpet appears in good agreement with all observations (section 3), and the resulting modeling explains the data (section 4). However, several questions remain unanswered.

5.2.1. Ductile deformation: lubrication or energy dissipation

It is unclear whether liquid-like state is a necessary condition for the formation of shark-fins. Liquefaction or fluidization is often emphasized for soft sediment deformation (e.g. Roche et al. 2013, Verhagen et al. 2013, Baas et al. 2014, 2016). Altogether, the shark-fins, slump and sediment-dike represent a form of deformation that can be seen as "ductile" for the granular bed as a whole. Numerous small-scale impact sags are present (e.g. Fig 7C), testifying that the bed was in a relatively uncompacted, metastable state shortly after deposition. If a liquefied or ductile state happens to be common at the base of pyroclastic currents, then this can have a dramatic lubrication effect and increase the runout distance of the whole flow.

However, the presence of shark-fins could also be a sign of increased dissipation. Indeed, shark-fins represent a shear component partitioned out of the flow into the bed via deformation. This process may be more effective in transferring energy than a turbulent boundary layer alone. Such an extra source of dissipation could thus efficiently decrease the runout distance. Further effort is necessary to understand these effects and scale them into boundary layer models for refined predictions of pyroclastic currents and sediment flows in general.

5.2.2. A skin effect

A second question concerns the size that shark-fin structures can achieve under a wave-and-shear mechanism. The thickness of deformation shall be related to the cohesion strength of the bed, which has to be high enough to achieve a transfer down into the substrate. The deeper the deformation, the more strength must be transferred, yet this is limited by how much shear the upper part of the substrate can support before losing its cohesion. Thus, shark-fins might be limited to a skin effect of a few centimeters. Most experimental work produced very small structures with a size comparable with our field examples (Rowley et al. 2011, Farin et al. 2014, Verhagen et al. 2013). Recently, Pollock et al. (2017) were able to vary the size of vortices formed during pneumatic granular experiments, yet produced structures no more than few centimeters in thickness. Other alternative explanations may be more relevant for meter-scale features producing overturning (see 5.1.2.)

5.2.3.Waning, depletive flows

Douillet et al. (2013b, 2018b) have suggested that the specific structural patterns of pyroclastic bedforms can be explained by a mechanism of "differential draping", whereby a depletive current deposits its load in a gentle current below the shear threshold for saltation. The presence of shark-fins fully supports this differential draping mechanism. Indeed, saltation cannot form shark-fins, and thus this threshold is unlikely to be achieved. Shark-fins are further likely related to transient depletive and waning (decelerating) conditions rather than a steady or uniform state (in the sense of Kneller and Branney 1995, Brown and Branney 2013). Indeed, the formation of traction carpets can be triggered by the oversaturation of a flow during waning (for an in-depth presentation of the saturation flux, see Andreotti et al. 2002, Charru et al. 2013). Further, patterns resembling shark-fins have only been documented for environments prone to rapid sedimentation and presence of traction carpets: turbidites, tsunamis or pyroclastic currents. Shark fins may thus be an indicator for highly laden, strongly waning flow, and it is speculated that they might also occur during strong floods as well as in paraglacial settings.

CONCLUSION

"Shark-fin" has been defined here as an umbrella term for structures with a local overturned nature confined to a narrow lateral extent. Such structures have been variously reported in the literature in deposits from turbidity currents, tsunamis and pyroclastic currents, as well as from granular flow experiments. Shark-fins are ubiquitous in the deposits of the dilute pyroclastic currents from the 2006 eruption of Tungurahua, with more than 220 structures inventoried over the 40 m^2 of sectioned outcrops.

The common association of shark-fins with erosive horizons points toward a syn-depositional mechanism. The overturning of shark-fins implies the coherent shearing of a stratal package by a basal granular flow. The spatial organization of shark-fins as repetitive periodic patterns along a single laminae suggests a conventional wave mechanism as trigger. Further observations highlight the lateral migration and concurrent growth of the structures during sedimentation, so that the growth rate of shark-fins should scale to the sedimentation rate of the flow.

A physical model whereby waves are triggered around a shear layer between the flow and bed was modified from the Holmboe instability problem, and appears adequate to explain the morphometric parameters of shark-fins. In particular, the stability analysis demonstrates that waves focused around a linear density and velocity gradients predict correctly the dimensions of shark-fins, which is not the case with a constant-density configuration. The calculated growth rates vary from 0.1-0.4 m/s, in good agreement with literature data from analogue experiments. Such high sedimentation rates support a model of pulsating sedimentation. All insights on the origin of shark-fins concur toward waves formed in a setting close to Holmboe instabilities whereas no convincing evidence, to our perception, supports the interpretation of these features as frozen Kelvin-Helmholtz instabilities. We foresee a risk of over-interpretation of shark-fins and overturned structures. Key observations are needed for an explanation involving wave-instabilities: (i) a stable spatial recurrence on a single horizon, (ii) signs of migration, and (iii) agreement of the wavelength over thickness ratio.

In the screening for shark-fins, other types of overturned patterns have been evidenced and interpreted as resulting from different processes. Structures resembling shark-fins were associated with sediment-dikes from a short intraflow as well as with a slump with short throw. During the eruption, the rapid sedimentation of a highly polydisperse mixture of clasts likely promoted the entrapment of consequent amounts of fluids, and so facilitated metastable conditions. This was probably an ideal ground for the onset of syn- and post-depositional soft sediment deformation and re-arrangements. Altogether, shark-fins and shear structures evidence a ductile-like deformation of the granular substrate, which could have consequent effects on the runout distance of a pyroclastic current. Whether this ductile-like bed acts as a lubricant, or helps to dissipate more energy through an increased transfer of shear into the ground remains to be explored.

Figure captions

Figure 1: A) Sketch of the general morphology of shark-fin patterns and the measurements carried. B) Sketch of "conventional overturned beds", reproduced from Allen and Banks (1972).

Figure 2: Position of shark-fins ("SF") within the sediment plate outcrops by types (color coded in the legend). Structures in-trains are linked by black lines. For large scale image and details on the outcrops, see Douillet et al. in-sub-b. The code for each plate gives the bedform type and transect number.

Figure 3: Sketch representing the three types of shark-fin patterns recognized in the outcrops. Pink lines: deformed beds, yellow lines: erosive contacts.

Figure 4: Convolute shark-fin structures. A. Train of 2 convolute shark-fins, the first one truncated by a major truncation and with an angular shape, the second composite with two nearby tails (Plate TrT1aP3, see Table in Annex 1). B. train of 2 convolute "bulbous" shark-fins downstream a crest. A fine-grained massive "ploughed" zone emanates directly above the shark-fins (Plate TrT2P5). C. Fine-grained and massive shark-fin in a disturbed zone (Plate LuTNP2). D. Singular coarse-grained angular shark-fin (Plate TrT4P6).

Figure 5: Truncated shark-fin structures. A-D Truncated ripple shark-fins: A. Plate TrT1aP4, B. Plate TrT1aP4, C. Plate TrP1aP3, D. Plate TrT3P6, E. Flat truncation shark-fins, Plate TrT1aP5.

Figure 6: Sketch representing the grouping and occurrence patterns of shark-fins.

Figure 7: In train shark-fin organization. A. shark-fin separated with regular occurrence (Plate LuT2P3-P4). B. shark-fin separated by increasing distance (Plate TrT2P3). C. Train organized downstream an erosive gully filled by backset-ripple beds (Plate TrT1aP3-4). D. shark-fin downstream crest knick-point on the top right, Steep overturning truncation on stoss face, train of shark-fin within disturbed zone in the middle right, impact sag on lower left part (Plate LuTNP2a).

Figure 8: Clusters of migrating shark-fin (migration followed with pink dotted lines). A. Overturned laminae can be followed climbing stratigraphy with an initially downstream migration followed by two step-backs (Plate TrT4P2). B. A cluster of shark-fins is preceded upstream by zones of ploughed laminae (see Douillet et al. 2015). C. Cluster climbing lamination in the downstream direction with succession of truncated-convolute-truncated shark-fins (Plate LuTNP5).

Figure 9: Distance separating shark-fins in single trains. A. Non corrected data B. Data with inter-distance halved or divided by three to account for missed harmonics. When divided, harmonics are represented by black crosses between full-occurrences.

Figure 10: Dimensions of shark-fin structures by types. Left side graphs are plotted versus length, right side versus thickness. The linear regressions are fitted by minimizing the euclidian distance between data and model after reducing and centering the data in order to account for the different length scales of the axes, and are calculated based on principal component analysis using the svd function in Matlab.

Figure 11: Irregular deformation zone. A. General view of lunate plate "LuT2" with deformed zones highlighted in pink. Location of figures B-E are highlighted by white boxes. B. Onset of deformation with scars underlined by overturned laminae, unconformable contact, and step-like lamination on the upper right in the deformed beds. C. Zone of compression with overturned beds. D. The top part of the bedform contains lineations that form steep backsets, ca. 1 cm-thick and with pattern followed over tens of centimeters laterally. E. Zone of compression with cluster of convolute laminae coexistent in disturbed to massive zones.

Figure 12: Sediment-dike structure. A. General view of Plate "Elongate" with location of deformation zone in Figure B marked with a white box. B. View of the sediment-dike structure. C. Zoom into the onset of deformation, chevron-like structures, and pickled basal surface

Figure 13: A) Interpretative sketch representing the process of formation of shark-fins. A turbulent flow develops a basal granular flow in the form of a thin traction carpet. There, a shear horizon occurs, and supports wave instabilities that rework the superficial bed and create shark-fins. B) Geometry of the physical framework used to model the formation of shark-fins.

Figure 14: Results of the stability analysis from the physical frameworks. Model with A. constant density, and B. linear density gradient. The color scale gives the growth rate of the wave instabilities as a function of the flow velocity (U_0) and ratio of wavelength over thickness of shear horizon (λ/d). Example for a shear horizon

of thickness d = 5 cm. C. Histogram for shark-fins "in-train" only of the recurrence interval (λ*) over thickness of deformation (H), thought to be the representation of the λ/d ratio. Large ratios likely represent harmonics (see Fig 9).

Figure 15: Gradient density model. Growth rate of the perturbation as a function of the Richardson number (Ri) and wavelength for a thickness of shear layer d = 3 cm. Inset: Comparison of the maximal growth zones for Kelvin-Helmholtz (KH, red) and Holmboe (blue) instabilities, redrawn from figure 5.3 in Lawrence et al. (2013).

Figure 16: Interpretative sketches for the alternative explanations. A) the slumping mechanism for the lunate outcrop. B) and C) The mechanism of deformation forming the sediment-dike via the intrusion of a dense granular flow within fine-grained metastable sediment.

Annex:

A1. Table of the shark-fin characteristics

Table caption A1:

Main characteristics of every encountered shark-fin structures.

plate code:

Lu (Lunate) or Tr (Transverse); T (Trench number); P (Plate number increasing from 1 to 6 in the downflow direction).

Affected zone & overlying beds:

-face- slope: S (Stoss), L (lee), F (Flat zone) C (Crest area). Slope is given in degree to the horizontal and positive when dipping against flow direction.

-Grain size (GS) attribute: (fin, mid, coa): fin: ~125 µm mid: 250 µm coa: 500 µm

-Stratification (strat) attribute: (CL / L / DL / M): crude and clear pronounced lamination (CL), normal well laminated (L), diffuse lamination only distinguishable with the impregnation method (DL) and massive (M).

-Additional lamination attribute: (DIST / W / BCKS / VERT / CHAOS): disturbed by deformation (DIST), Wavy laminasets (W), backset laminae (BCKS), vertical backset bedding (VERT), chaotic zone with hardly interpretable reason (CHAOS)

-Additional lamina(DIST / W / BCKS / VERT / CHAOS): disturbed by deformation (DIST), Wavy laminasets (W), backset laminae (BCKS), vertical backset bedding (VERT), chaotic zone with hardly interpretable reason (CHAOS)

Overturned structure:

L (Length of affected zone), T (Thickness of affected zone), N lam (Number of affected laminae), E (Elongation) D-next (Distance to next shark-fin, if in-train)

Upper contact:

Slope angle and Type: erosive (ER) or concordant (C)

Lateral continuity & Comments:

Same abbreviations as for the rest of table

Position:

Measured from upstream end of plate, vertical (vert) and horizontal (hor) position, as well as position within the 2006 sequence (seq): base (B), middle (M) or top (T).

A2. Physical framework

(separated document ANNEX2_Equations.docx)

Acknowledgements

Matthieu Cartigny and Vern Manville are acknowledged gratefully for their critical reading of an earlier version of the manuscript. GAD acknowledges funding of this project by the Deutsche Forschungsgemeinschaft grant DO1953/1-1. Several tests were done during a campaign funded by the "BayLat" agency to GAD (Bavaria-Latin-America exchange program). QC was funded by the Alsacian grant "Boussole" for his internship. M. Bouysson, I Holscher, R. Reschetizka and P. Witting worked as student assistants to mount the sediment plate exhibition through the "LMU-StudiForscht" funding scheme. DBD wishes to acknowledge the support of an ERC Advanced Grant (247076).

References

Allen, J. R. L., & Banks, N. L. (1972). An interpretation and analysis of recumbent-folded deformed cross-bedding. Sedimentology, 19(3-4), 257-283.

Allen J.R.L. (1982). Sedimentary structures, their character and physical basis (Vol. 2). Developments in Sedimentology 30B. Elsevier.

Alsop, G. I., & Holdsworth, R. E. (2006). Sheath folds as discriminators of bulk strain type. Journal of Structural Geology, 28(9), 1588-1606.

Alsop, G. I., Holdsworth, R. E., & McCaffrey, K. J. W. (2007). Scale invariant sheath folds in salt, sediments and shear zones. Journal of Structural Geology, 29(10), 1585-1604.

Andreotti, B., Claudin, P., & Douady, S. (2002). Selection of dune shapes and velocities Part 1: Dynamics of sand, wind and barchans. The European Physical Journal B-Condensed Matter and Complex Systems, 28(3), 321-339.

Baas, J. H., Manica, R., Puhl, E., Verhagen, I., & Borges, A. L. D. O. (2014). Processes and products of turbidity currents entering soft muddy substrates. Geology, 42(5), 371-374.

Baas, J. H., Manica, R., Puhl, E., & Oliveira Borges, A. L. (2016). Thresholds of intrabed flow and other interactions of turbidity currents with soft muddy substrates. Sedimentology, 63(7), 2002-2036.

Benage, M. C., Dufek, J., Degruyter, W., Geist, D., Harpp, K., & Rader, E. (2014). Tying textures of breadcrust bombs to their transport regime and cooling history. Journal of Volcanology and Geothermal Research, 274, 92-107.

Benage, M. C., Dufek, J., & Mothes, P. A. (2016). Quantifying entrainment in pyroclastic density currents from the Tungurahua eruption, Ecuador: Integrating field proxies with numerical simulations. Geophysical Research Letters, 43(13), 6932-6941.

Benjamin, T. B., & Mullin, T. (1988). Buckling instabilities in layers of viscous liquid subjected to shearing. Journal of Fluid Mechanics, 195, 523-540.

Bernard, J., Kelfoun, K., Le Pennec, J. L., & Vargas, S. V. (2014). Pyroclastic flow erosion and bulking processes: comparing field-based vs. modeling results at Tungurahua volcano, Ecuador. Bulletin of volcanology, 76(9), 858.

Brand, B. D., Pollock, N., Sarocchi, D., Dufek, J., & Clynne, M. A. (2017). Field-trip guide for exploring pyroclastic density current deposits from the May 18, 1980, eruption of Mount St. Helens, Washington (No. 2017-5022-C). US Geological Survey.

Branney, M. J., & Kokelaar, B. P. (1992). A reappraisal of ignimbrite emplacement: progressive aggradation and changes from particulate to non-particulate flow during emplacement of high-grade ignimbrite. Bulletin of Volcanology, 54, 504-520.

Branney, M. J., & Kokelaar, B. P. (2002). Pyroclastic density currents and the sedimentation of ignimbrites. Geological Society of London.

Branney, M. J., Barry, T. L., & Godchaux, M. (2004). Sheathfolds in rheomorphic ignimbrites. Bulletin of Volcanology, 66(6), 485-491.

Breard, E. C., Lube, G., Jones, J. R., Dufek, J., Cronin, S. J., Valentine, G. A., & Moebis, A. (2016). Coupling of turbulent and non-turbulent flow regimes within pyroclastic density currents. Nature Geoscience, 9(10), 767-771.

Breard, E. C., & Lube, G. (2017). Inside pyroclastic density currents–uncovering the enigmatic flow structure and transport behaviour in large-scale experiments. Earth and Planetary Science Letters, 458, 22-36.

Brown, R.J. & Branney, M.J. (2013) Internal □ow variations and diachronous sedimentation within extensive, sustained, density-strati □ ed pyroclastic density currents □ owing down gentle slopes, as revealed by the internal architectures of ignimbrites on Tenerife., Bull. Volcanol.., 75 (7). p. 727.

Burgisser, A., & Bergantz, G. W. (2002). Reconciling pyroclastic flow and surge: the multiphase physics of pyroclastic density currents. Earth and Planetary Science Letters, 202(2), 405-418.

Butler, R. W., & Tavarnelli, E. (2006). The structure and kinematics of substrate entrainment into high-concentration sandy turbidites: a field example from the Gorgoglione 'flysch'of southern Italy. Sedimentology, 53(3), 655-670.

Butler, R. W., Eggenhuisen, J. T., Haughton, P., & McCaffrey, W. D. (2016). Interpreting syndepositional sediment remobilization and deformation beneath submarine gravity flows; a kinematic boundary layer approach. Journal of the Geological Society, 173(1), 46-58.

Carreras, J., & Druguet, E. (2018). Complex fold patterns developed by progressive deformation. Journal of Structural Geology.

Chan, M. A. and Bruhn, R. L. (2014). Dynamic liquefaction of Jurassic sand dunes: processes, Origins, and implications, Earth Surf. Proc. Land., 39, 1478–1491.

Charru, F., Andreotti, B., & Claudin, P. (2013). Sand ripples and dunes. Annual Review of Fluid Mechanics, 45, 469-493.

Cobbold, P. R., & Quinquis, H. (1980). Development of sheath folds in shear regimes. Journal of structural geology, 2(1-2), 119-126.

Cole, P. D. (1991). Migration direction of sand-wave structures in pyroclastic-surge deposits: implications for depositional processes. Geology, 19(11), 1108-1111.

Cole, P. D., Guest, J. E., & Duncan, A. M. (1993). The emplacement of intermediate volume ignimbrites: a case study from Roccamonfina Volcano, Southern Italy. Bulletin of Volcanology, 55(7), 467-480.

Crowe, B. M., & Fisher, R. V. (1973). Sedimentary structures in base-surge deposits with special reference to cross-bedding, Ubehebe Craters, Death Valley, California. Geological Society of America Bulletin, 84(2), 663-682.

Dellino, P., Isaia, R., & Veneruso, M. (2004). Turbulent boundary layer shear flows as an approximation of base surges at Campi Flegrei (Southern Italy). Journal of Volcanology and Geothermal Research, 133(1), 211-228.

Douillet, G. A., Tsang-Hin-Sun, È., Kueppers, U., Letort, J., Pacheco, D. A., Goldstein, F., ... & Robin, C. (2013a). Sedimentology and geomorphology of the deposits from the August 2006 pyroclastic density currents at Tungurahua volcano, Ecuador. Bulletin of volcanology, 75(11), 765.

Douillet, G. A., Pacheco, D. A., Kueppers, U., Letort, J., Tsang-Hin-Sun, È., Bustillos, J., ... & Dingwell, D. B. (2013b). Dune bedforms produced by dilute pyroclastic density currents from the August 2006 eruption of Tungurahua volcano, Ecuador. Bulletin of volcanology, 75(11), 762.

Douillet, G. A., Rasmussen, K. R., Kueppers, U., Castro, D. L., Merrison, J. P., Iversen, J. J., & Dingwell, D. B. (2014). Saltation threshold for pyroclasts at various bedslopes: Wind tunnel measurements. Journal of Volcanology and Geothermal Research, 278, 14-24.

Douillet, G. A., Taisne, B., Müller, S. K., Kueppers, U., & Dingwell, D. B. (2015). Syn-eruptive, soft-sediment deformation of deposits from dilute pyroclastic density current: triggers from granular shear, dynamic pore pressure, ballistic impacts and shock waves. Solid Earth, 6(2), 553.

Douillet, G. A., Bouysson, M., Gegg, L., (2017). Overturned strata in deposits of dilute pyroclastic density currents, field and analogue data. Abstract 1228. IAVCEI Scientific Assembly, Portland Oregon, 14-18.08.2017.

Douillet G.A., Kueppers U., Mato C. Bouysson M., Chaffaut Q., Reschetizka R., Dingwell D.B., Bernard B. (2018) Revisiting the lacquer peels method with pyroclastic deposits: sediment plates, a precise, fine-scale imaging method and powerful outreach tool. Journal of Applied Volcanology 7:11 https://doi.org/10.1186/s13617-018-0080-2

Douillet G.A., Bernard B., Bouysson M., Chaffaut Q., Dingwell D.B., Gegg L., Holscher I., Kueppers U., Mato C., Ritz V.A., Schlunegger F., Witting P. (2018/2019). Pyroclastic dune bedforms: macroscale structures and lateral variations. Examples from the 2006 pyroclastic currents at Tungurahua (Ecuador). Sedimentology (some future issue?) doi: 10.1111/sed.12542

Dufek J, Bergantz GW. (2007). Suspended load and bed-load transport of particle-laden gravity currents: the role of particle–bed interaction. Theor. Comput. Fluid Dyn. 21:119–4

Dufek, J. (2016). The fluid mechanics of pyroclastic density currents. Annual Review of Fluid Mechanics, 48, 459-485.

Eggenhuisen, J. T., McCaffrey, W. D., Haughton, P. D., & Butler, R. W. (2011). Shallow erosion beneath turbidity currents and its impact on the architectural development of turbidite sheet systems. Sedimentology, 58(4), 936-959.

Farin, M., Mangeney, A., & Roche, O. (2014). Fundamental changes of granular flow dynamics, deposition, and erosion processes at high slope angles: insights from laboratory experiments. Journal of Geophysical Research: Earth Surface, 119(3), 504-532.

Fisher, R. V. (1979). Models for pyroclastic surges and pyroclastic flows. Journal of Volcanology and Geothermal Research, 6(3-4), 305-318.

Gladstone, C., & Sparks, R. S. J. (2002). The significance of grain-size breaks in turbidites and pyroclastic density current deposits. Journal of Sedimentary Research, 72(1), 182-191.

Gladstone, C., Ritchie, L. J., Sparks, R. S. J., & Woods, A. W. (2004). An experimental investigation of density-stratified inertial gravity currents. Sedimentology, 51(4), 767-789.

Gladstone, C., McClelland, H. M. O., Woodcock, N. H., Pritchard, D., & Hunt, J. (2017). On the formation of convolute lamination in mud-rich turbidites. Sedimentology, 1-43.

Goldfarb, D. J., Glasser, B. J., & Shinbrot, T. (2002). Shear instabilities in granular flows. Nature, 415(6869), 302-305.

Horowitz, D. H. (1982). Geometry and origin of large-scale deformation structures in some ancient wind-blown sand deposits. Sedimentology, 29(2), 155-180.

Houssais, M., Ortiz, C. P., Durian, D. J., & Jerolmack, D. J. (2015). Onset of sediment transport is a continuous transition driven by fluid shear and granular creep. Nature communications, 6.

Kelfoun, K., Samaniego, P., Palacios, P., & Barba, D. (2009). Testing the suitability of frictional behaviour for pyroclastic flow simulation by comparison with a well-constrained eruption at Tungurahua volcano (Ecuador). Bulletin of volcanology, 71(9), 1057.

Kneller, B. C. & Branney, M. J. (1995). Sustained high-density turbidity currents and the deposition of thick massive sands. Sedimentology, 42, 607-616.

Kneller, B., & Buckee, C. (2000). The structure and fluid mechanics of turbidity currents: a review of some recent studies and their geological implications. Sedimentology, 47, 62-94.

Larsen, P. H. (1986). Soft sediment deformation structures in Silurian turbidites from North Greenland. Bull. Geol. Soc. Denmark, 35, 19-23.

Lawrence, G.A., Tedford, E.D. & Carpenter, J.R. (2013). Instabilities in Stratified Shear Flow. Coherent flow structures at earth's surface, 63-71.

Logan, W.E., 1863. Report on the Geology of Canada. John Lovell, Montreal, Canada, p. 464.

Lowe, D. R. (1976). Subaqueous liquefied and fluidized sediment flows and their deposits. Sedimentology, 23(3), 285-308.

Lube, G., Cronin, S. J., Platz, T., Freundt, A., Procter, J. N., Henderson, C., & Sheridan, M. F. (2007). Flow and deposition of pyroclastic granular flows: A type example from the 1975 Ngauruhoe eruption, New Zealand. Journal of Volcanology and Geothermal Research, 161(3), 165-186.

Maltman, A. (Ed.). (1994). The geological deformation of sediments. Springer Science & Business Media, Springer, Dordrecht

Marques (2012) Comment on “Eye and sheath folds in turbidite convolute lamination: Aberystwyth Grits Group, Wales”, by H.L.O. McClelland, N.H. Woodcock, C. Gladstone, Journal of Structural Geology 33 (2011) 1140–1147. Journal of Structural Geology, 37, 248-250

McClelland, H. L. O., Woodcock, N. H., & Gladstone, C. (2011). Eye and sheath folds in turbidite convolute lamination: Aberystwyth Grits Group, Wales. Journal of Structural Geology, 33(7), 1140-1147.

McKee, E. D., Reynolds, M. A., & Baker Jr, C. H. (1962a). 164. Laboratory studies on deformation in unconsolidated sediment. US Geological Survey Professional Paper, 151.

McKee, E. D., Reynolds, M. A., & Baker Jr, C. H. (1962b). 165. Experiments on intraformational recumbent folds in cross bedded sand. US Geological Survey Professional Paper, 155.

Menczel, A., & Kostaschuk, R. (2013). Interfacial waves as coherent flow structures associated with continuous turbidity currents: Lillooet Lake, Canada. Coherent flow structures at earth's surface, 371-383.

Mitrano, P. P., Garzó, V., Hilger, A. M., Ewasko, C. J., & Hrenya, C. M. (2012). Assessing a hydrodynamic description for instabilities in highly dissipative, freely cooling granular gases. Physical Review E, 85(4), 041303.

Morgenthaler J., Frehner M. (2017). Bulldozer-like soil erosion at the front of a rockglacier indicates change in advance dynamics: Case study from the Furggentälti, Vallais, Switzerland. Swiss Geoscience Meeting, Davos 18.11.2017

Nichol, K., Zanin, A., Bastien, R., Wandersman, E. & van Hecke, M. Flow-induced agitations create a granular fluid. Phys. Rev. Lett. 104, 078302 (2010).

Ongaro, T. E., Neri, A., Menconi, G., Vitturi, M. D. M., Marianelli, P., Cavazzoni, C., ... & Baxter, P. J. (2008). Transient 3D numerical simulations of column collapse and pyroclastic density current scenarios at Vesuvius. Journal of Volcanology and Geothermal Research, 178(3), 378-396.

Ongaro, T. E., Widiwijayanti, C., Clarke, A. B., Voight, B., & Neri, A. (2011). Multiphase-flow numerical modeling of the 18 May 1980 lateral blast at Mount St. Helens, USA. Geology, 39(6), 535-538.

Owen, G., Moretti, M., & Alfaro, P. (2011). Recognising triggers for soft-sediment deformation: current understanding and future directions. Sedimentary Geology, 235(3), 133-140.

Palladino, D. M. (2017). Simply pyroclastic currents. Bulletin of Volcanology, 79(7), 53.

Parejas, C. S., Druitt, T. H., Robin, C., Moreno, H., & Naranjo, J. A. (2010). The Holocene Pucón eruption of Volcán Villarrica, Chile: deposit architecture and eruption chronology. Bulletin of volcanology, 72(6), 677-692.

Pollock N., Brand B., Roche O., Rowley P., Sarocchi D., Sulpizio R. (2017). Using shear-induced, wave-like depositional features to infer flow conditions of pyroclastic density currents at Mount St Helens, Washington, USA. Abstract 1081. IAVCEI Scientific Assembly, Portland Oregon, 14-18.08.2017.

Postma, G., Cartigny, M., & Kleverlaan, K. (2009). Structureless, coarse-tail graded Bouma Ta formed by internal hydraulic jump of the turbidity current?. Sedimentary Geology, 219(1), 1-6.

Postma, G., Kleverlaan, K., & Cartigny, M. J. (2014). Recognition of cyclic steps in sandy and gravelly turbidite sequences, and consequences for the Bouma facies model. Sedimentology, 61(7), 2268-2290.

Rader, E., Geist, D., Geissman, J., Dufek, J., & Harpp, K. (2015). Hot clasts and cold blasts: thermal heterogeneity in boiling-over pyroclastic density currents. Geological Society, London, Special Publications, 396(1), 67-86.

Rowley, P. J., Kokelaar, P., Menzies, M., & Waltham, D. (2011). Shear-derived mixing in dense granular flows. Journal of Sedimentary Research, 81(12), 874-884.

Rowley, P. (2010). Analogue modelling of pyroclastic density current deposition (Doctoral dissertation, Royal Holloway, University of London).

Roche, O., Niño, Y., Mangeney, A., Brand, B., Pollock, N., & Valentine, G. A. (2013). Dynamic pore-pressure variations induce substrate erosion by pyroclastic flows. Geology, 41(10), 1107-1110.

Shanmugam, G. (2017). Global case studies of soft-sediment deformation structures (SSDS): Definitions, classifications, advances, origins, and problems. Journal of Palaeogeography, 6(4), 251-320.

Sohn, Y. K. (1997). On traction-carpet sedimentation. Journal of Sedimentary Research, 67(3).

Smyth, W. D. and Winters, K.B. (2003) Turbulence and mixing in Holmboe waves. Journal of Physical Oceanography 33, 694– 711.

Sparks, R. S. J. (1976). Grain size variations in ignimbrites and implications for the transport of pyroclastic flows. Sedimentology, 23(2), 147-188.

Strachan, L. J., & Alsop, G. I. (2006). Slump folds as estimators of palaeoslope: a case study from the Fisherstreet Slump of County Clare, Ireland. Basin Research, 18(4), 451-470.

Sulpizio, R., Mele, D., Dellino, P., & La Volpe, L., (2007). High variability of sedimentology and physical properties of pyroclastic density currents during complex Subplinian eruptions: the example of the AD 472 (Pollena) eruption of Somma-Vesuvius, Italy. Sedimentology, 54, 607–635.

Sulpizio, R., Dellino, P., Doronzo, D. M., & Sarocchi, D. (2014). Pyroclastic density currents: state of the art and perspectives. Journal of Volcanology and Geothermal Research, 283, 36-65.

Sulpizio R., Sarocchi D., Rodriguez-Sedano L. A., Brand B., Pollock N., Campos G. (2017). On the entrapment mechanisms of volcanic granular flows from laboratory experiments and comparison with natural exposures. Abstract 827. IAVCEI Scientific Assembly, Portland Oregon, 14-18.08.2017.

Taboada, A., Chang, K. J., Radjaï, F., & Bouchette, F. (2005). Rheology, force transmission, and shear instabilities in frictional granular media from biaxial numerical tests using the contact dynamics method. Journal of Geophysical Research: Solid Earth, 110(B9).

Verhagen, I. T. E., Baas, J. H., Jacinto, R. S., McCaffrey, W. D., & Davies, A. G. (2013). A first classification scheme of flow-bed interaction for clay-laden density currents and soft substrates. Ocean Dynamics, 63(4), 385-397.

Sutherland, B. R. (2005). Stratified shear flow: instability and wave radiation. WIT Transactions on State-of-the-art in Science and Engineering, 6.

Walker, G. P. (1984). Characteristics of dune-bedded pyroclastic surge bedsets. Journal of Volcanology and Geothermal Research, 20(3-4), 281-296.

Wohletz, K. H., & Sheridan, M. F. (1979). A model of pyroclastic surge. Geological Society of America Special Papers, 180, 177-194.

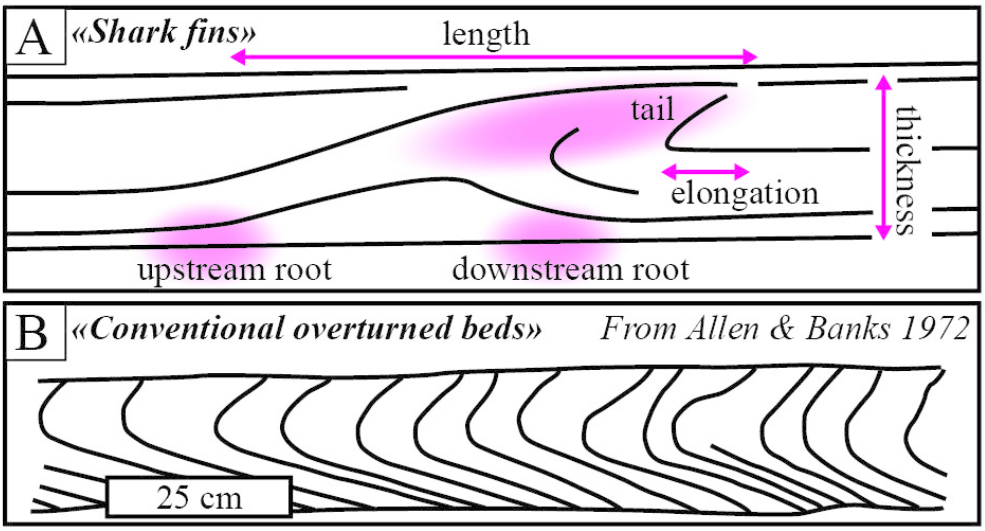

A) Sketch of the general morphology of shark-fin patterns and the measurements carried. B) Sketch of "conventional overturned beds", reproduced from Allen and Banks (1972).

80x42mm (300 x 300 DPI)

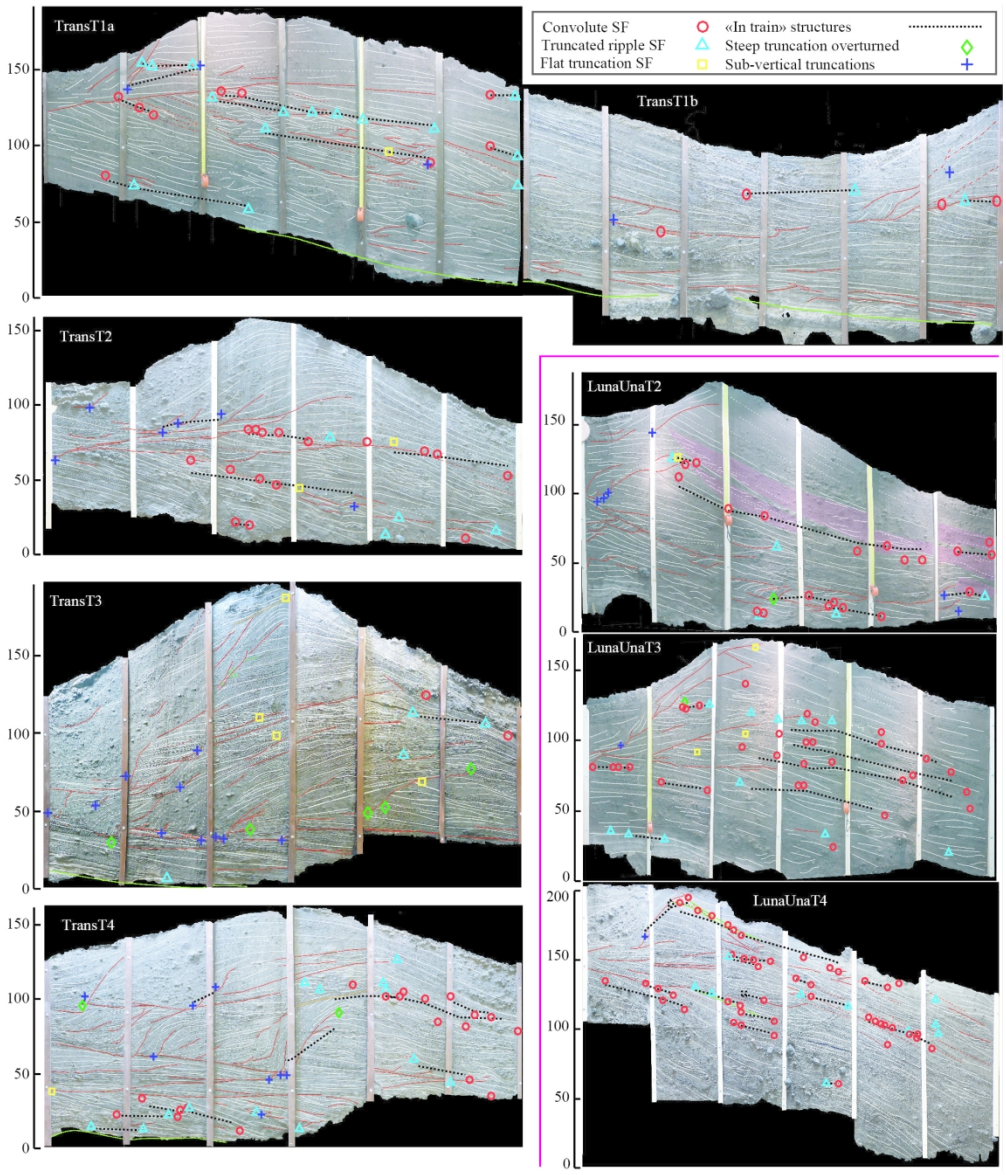

osition of shark-fins ("SF") within the sediment plate outcrops by types (color coded in the legend). Structures in-trains are linked by black lines. For large scale image and details on the outcrops, see Douillet et al. in-sub-b. The code for each plate gives the bedform type and transect number.

180x209mm (300 x 300 DPI)

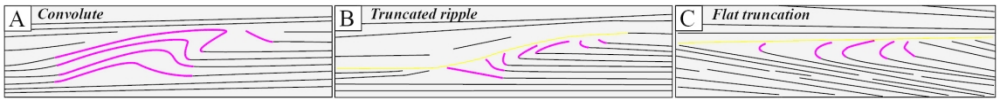

Sketch representing the three types of shark-fin patterns recognized in the outcrops. Pink lines: deformed beds, yellow lines: erosive contacts.

180x18mm (300 x 300 DPI)

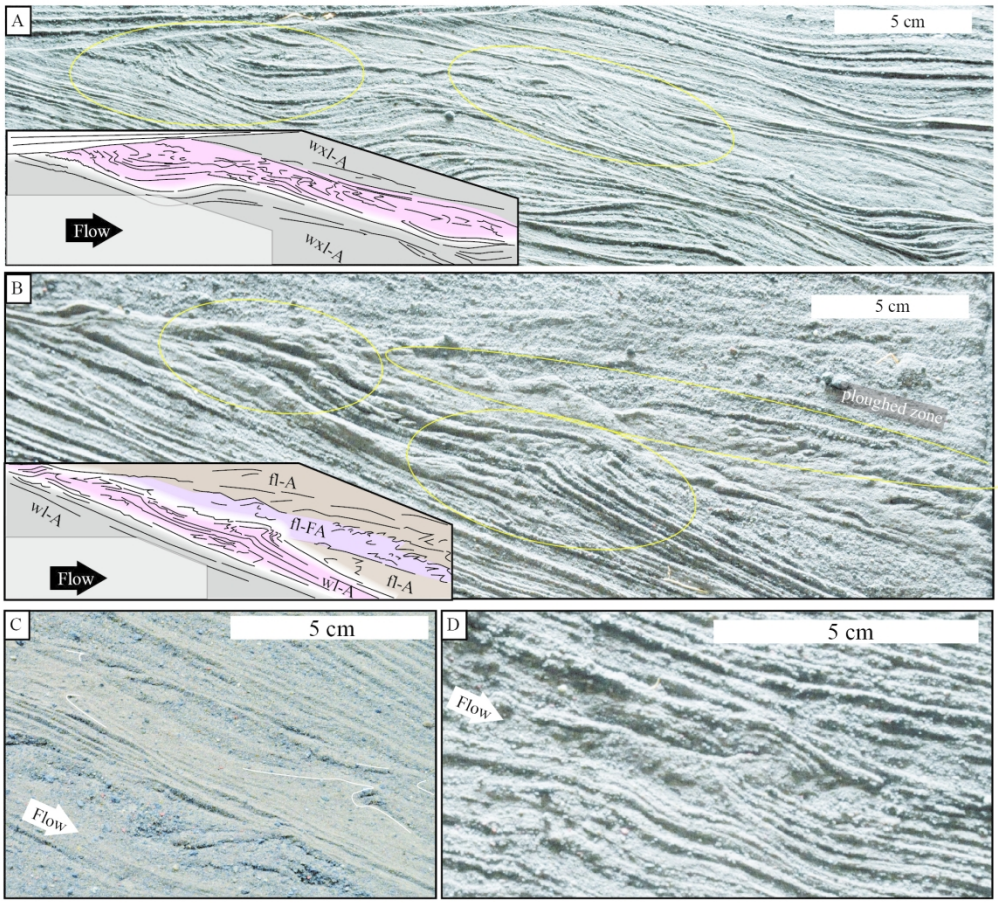

Convolute shark-fin structures. A. Train of 2 convolute shark-fins, the first one truncated by a major truncation and with an angular shape, the second composite with two nearby tails (Plate TrT1aP3, see Table in Annex 1). B. train of 2 convolute "bulbous" shark-fins downstream a crest. A fine-grained massive "ploughed" zone emanates directly above the shark-fins (Plate TrT2P5). C. Fine-grained and massive shark-fin in a disturbed zone (Plate LuTNP2). D. Singular coarse-grained angular shark-fin (Plate TrT4P6).

180x162mm (300 x 300 DPI)

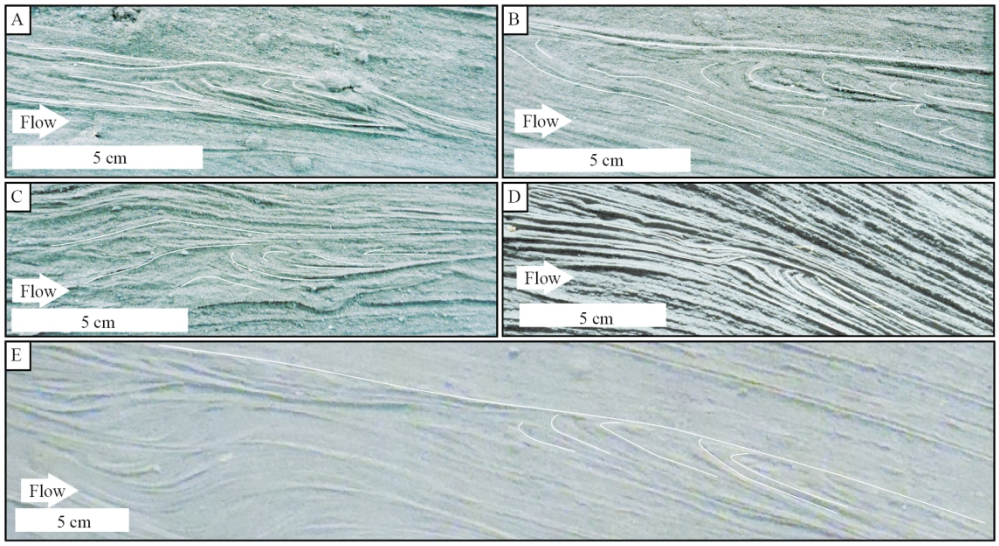

Truncated shark-fin structures. A-D Truncated ripple shark-fins: A. Plate TrT1aP4, B. Plate TrT1aP4, C. Plate TrP1aP3, D. Plate TrT3P6, E. Flat truncation shark-fins, Plate TrT1aP5.

180x97mm (300 x 300 DPI)

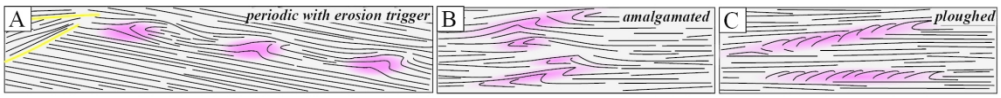

Sketch representing the grouping and occurrence patterns of shark-fins.

180x16mm (300 x 300 DPI)

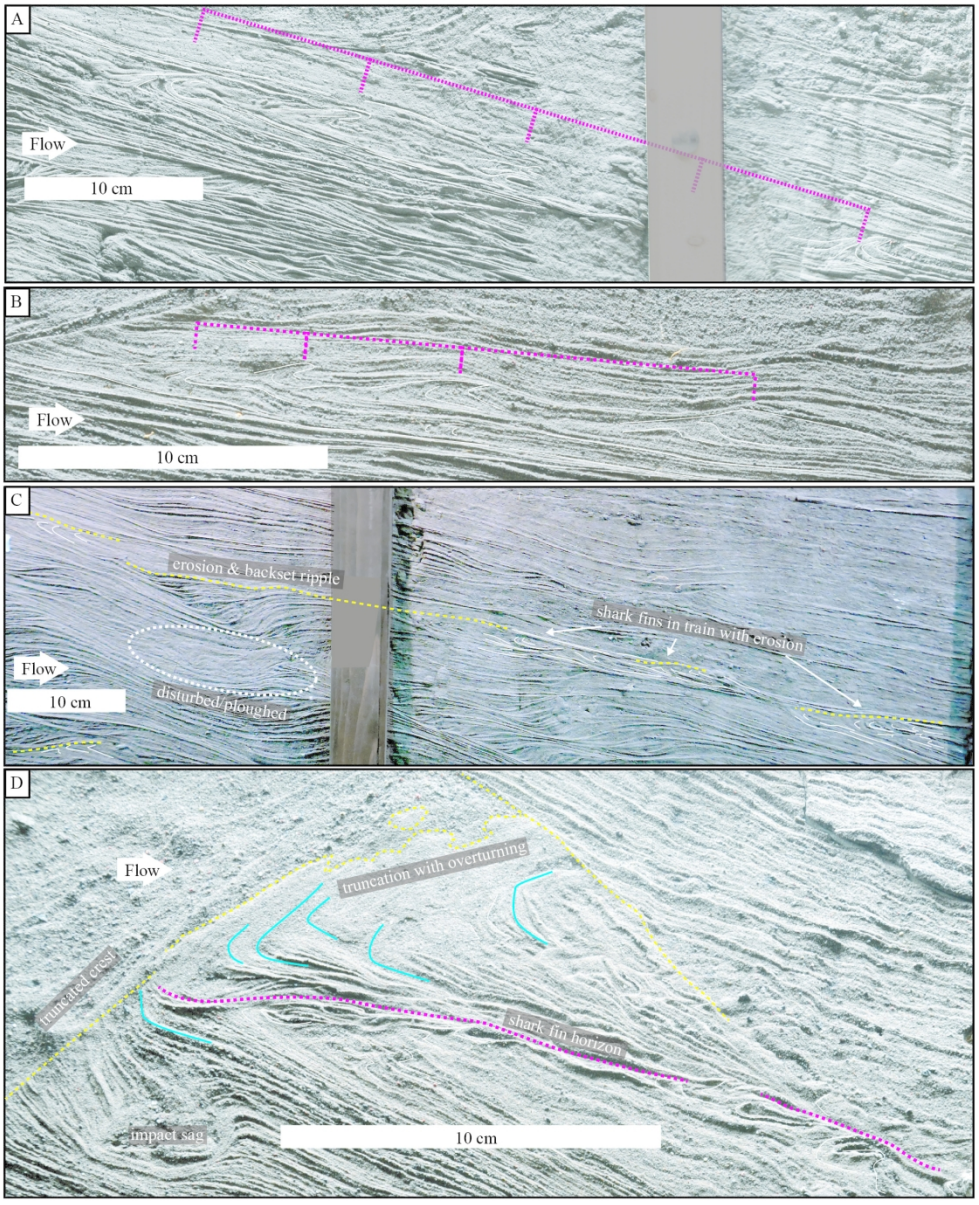

In train shark-fin organization. A. shark-fin separated with regular occurrence (Plate LuT2P3-P4). B. shark-fin separated by increasing distance (Plate TrT2P3). C. Train organized downstream an erosive gully filled by backset-ripple beds (Plate TrT1aP3-4). D. shark-fin downstream crest knick-point on the top right, Steep overturning truncation on stoss face, train of shark-fin within disturbed zone in the middle right, impact sag on lower left part (Plate LuTNP2a).

180x219mm (300 x 300 DPI)

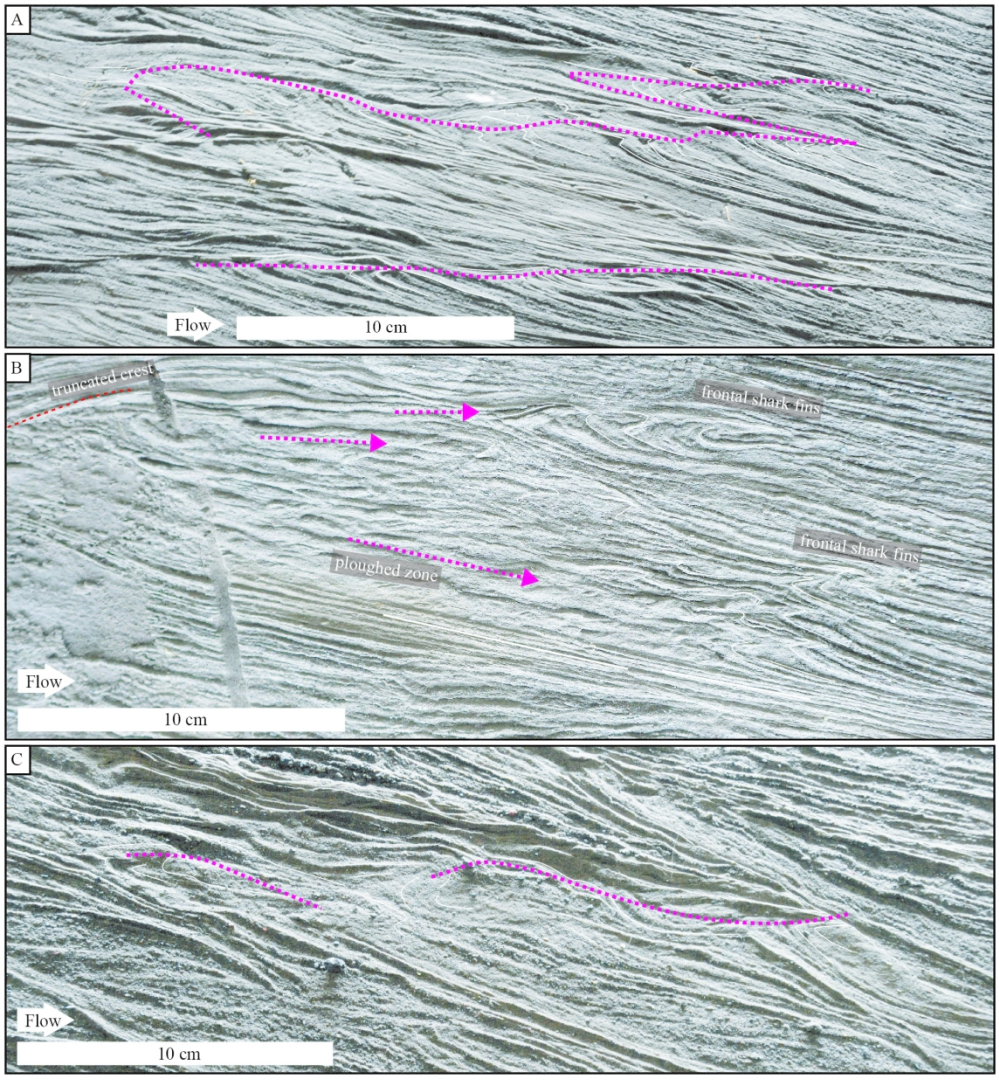

Clusters of migrating shark-fin (migration followed with pink dotted lines). A. Overturned laminae can be followed climbing stratigraphy with an initially downstream migration followed by two step-backs (Plate TrT4P2). B. A cluster of shark-fins is preceded upstream by zones of ploughed laminae (see Douillet et al. 2015). C. Cluster climbing lamination in the downstream direction with succession of truncated-convolute-truncated shark-fins (Plate LuTNP5).

180x193mm (300 x 300 DPI)

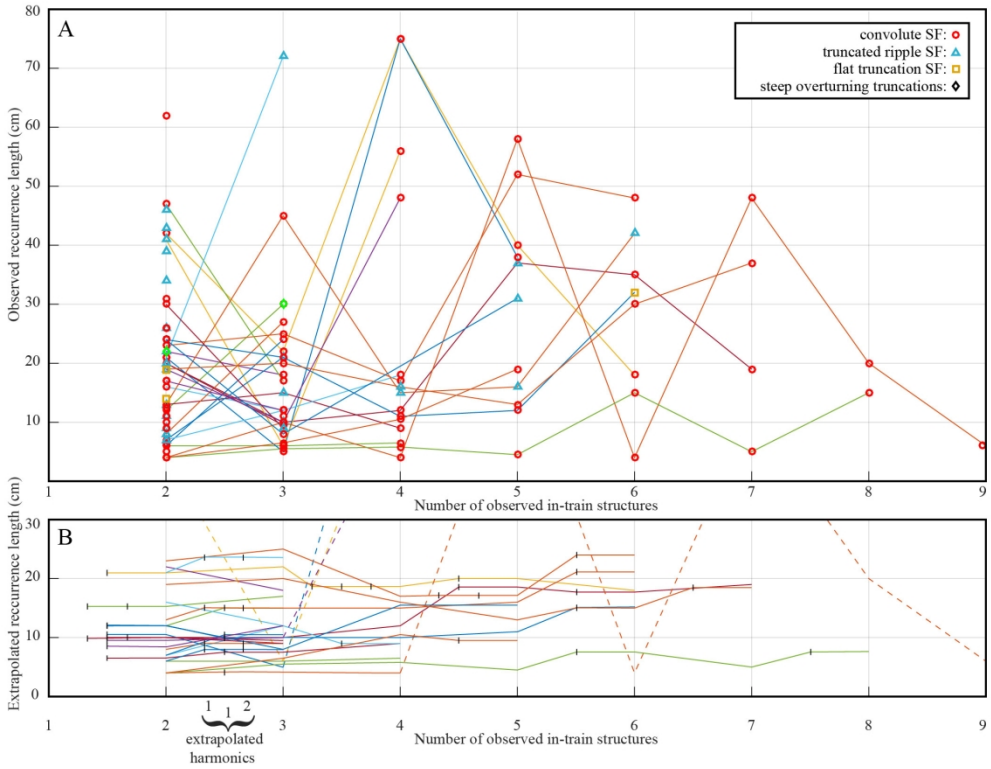

Distance separating shark-fins in single trains. A. Non corrected data B. Data with inter-distance halved or divided by three to account for missed harmonics. When divided, harmonics are represented by black crosses between full-occurrences.

180x140mm (300 x 300 DPI)

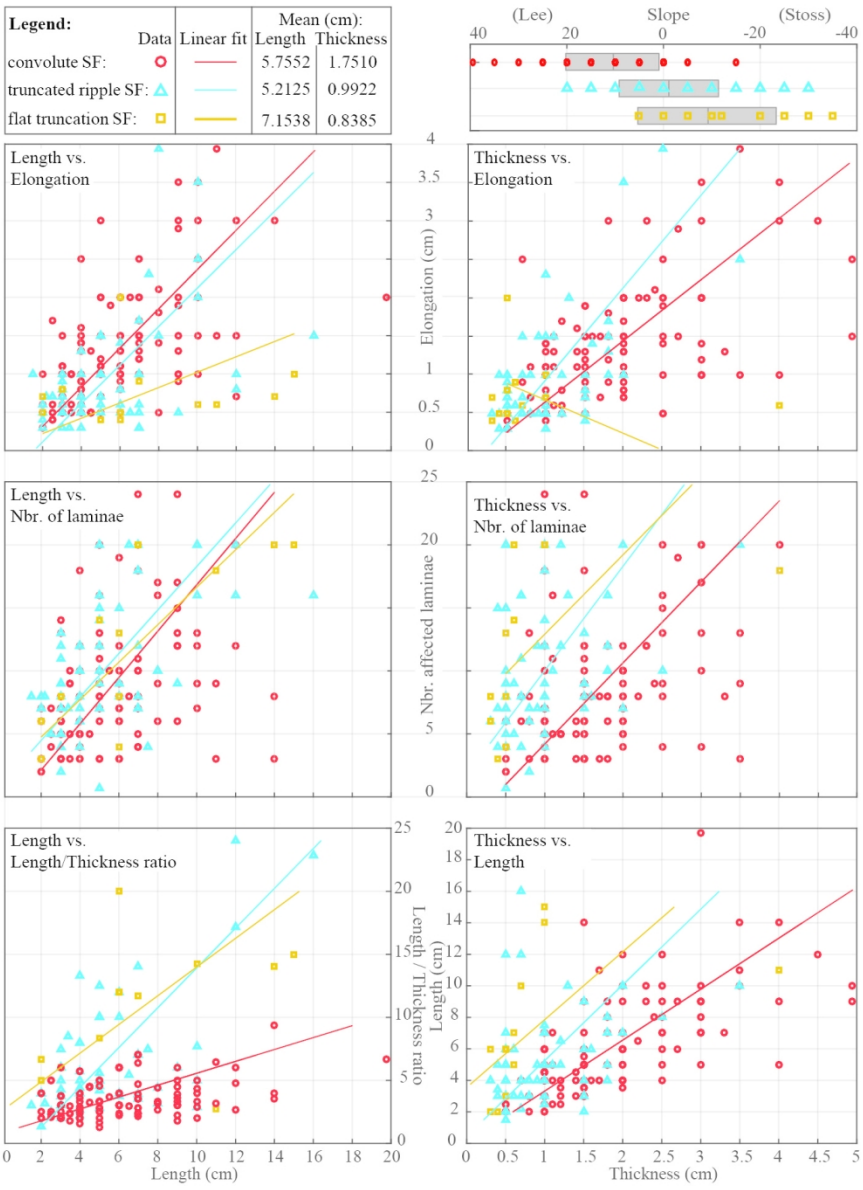

Dimensions of shark-fin structures by types. Left side graphs are plotted versus length, right side versus thickness. The linear regressions are fitted by minimizing the euclidian distance between data and model after reducing and centering the data in order to account for the different length scales of the axes, and are calculated based on principal component analysis using the svd function in Matlab.

119x165mm (300 x 300 DPI)

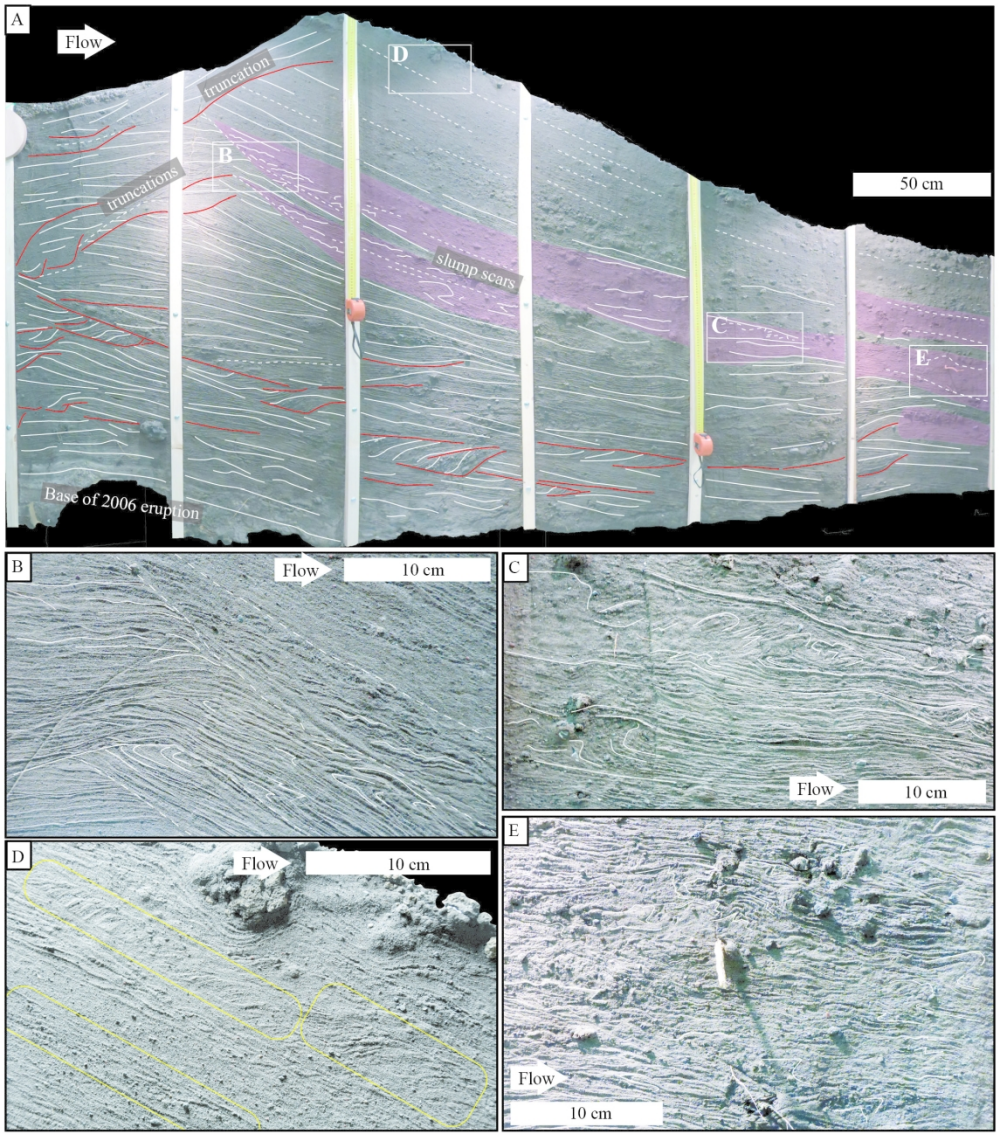

Irregular deformation zone. A. General view of lunate plate "LuT2" with deformed zones highlighted in pink. Location of figures B-E are highlighted by white boxes. B. Onset of deformation with scars underlined by overturned laminae, unconformable contact, and step-like lamination on the upper right in the deformed beds. C. Zone of compression with overturned beds. D. The top part of the bedform contains lineations that form steep backsets, ca. 1 cm-thick and with pattern followed over tens of centimeters laterally. E. Zone of compression with cluster of convolute laminae coexistent in disturbed to massive zones.

180x204mm (300 x 300 DPI)

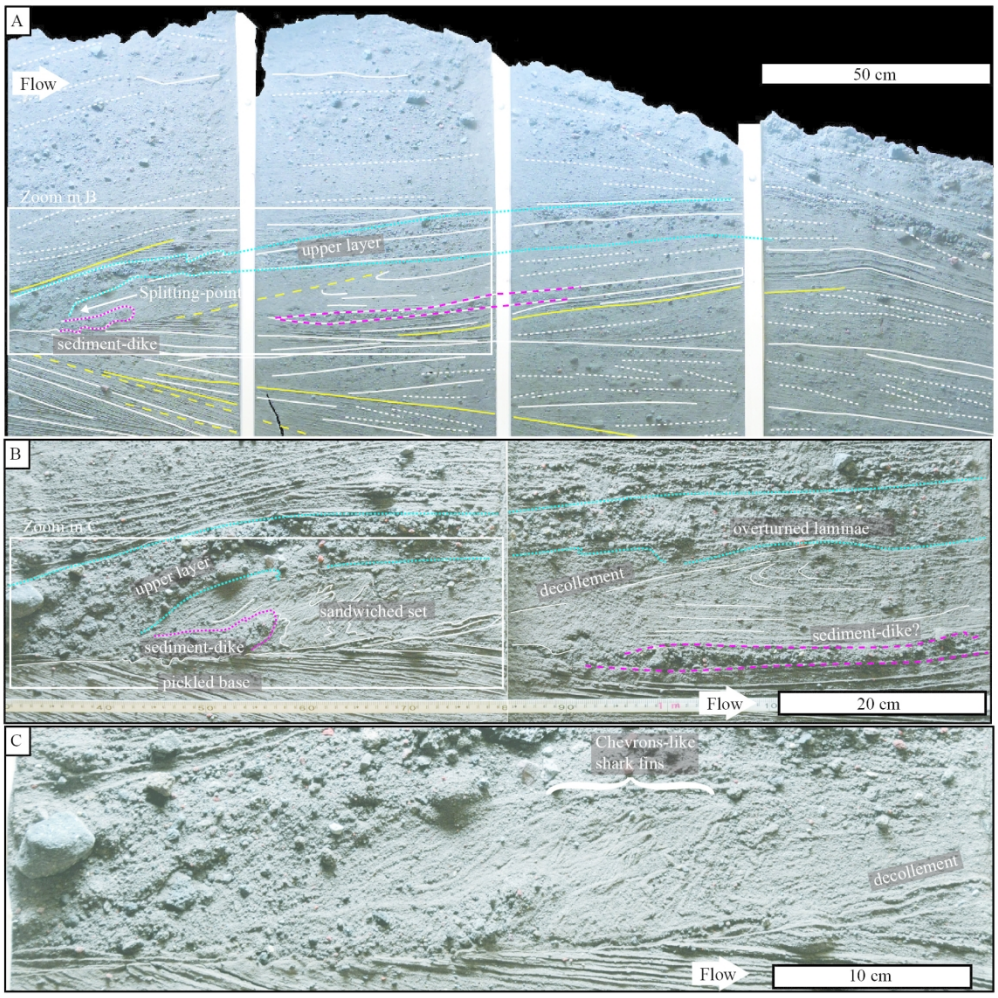

Sediment-dike structure. A. General view of Plate "Elongate" with location of deformation zone in Figure B marked with a white box. B. View of the sediment-dike structure. C. Zoom into the onset of deformation, chevron-like structures, and pickled basal surface.

180x180mm (300 x 300 DPI)

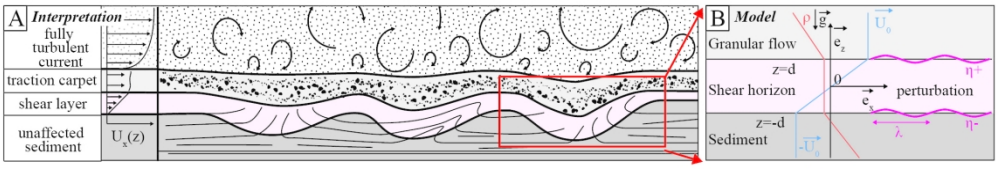

A) Interpretative sketch representing the process of formation of shark-fins. A turbulent flow develops a basal granular flow in the form of a thin traction carpet. There, a shear horizon occurs, and supports wave instabilities that rework the superficial bed and create shark-fins. B) Geometry of the physical framework used to model the formation of shark-fins.

180x30mm (300 x 300 DPI)

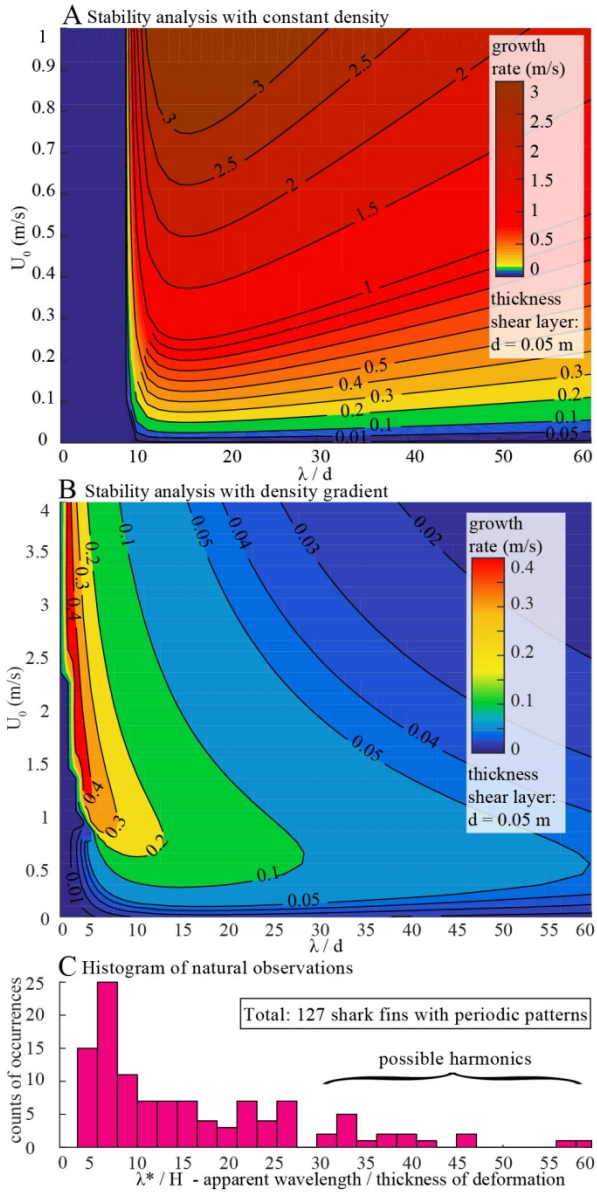

Results of the stability analysis from the physical frameworks. Model with A. constant density, and B. linear density gradient. The color scale gives the growth rate of the wave instabilities as a function of the flow velocity (U0) and ratio of wavelength over thickness of shear horizon (λ/d). Example for a shear horizon of thickness d = 5 cm. C. Histogram for shark-fins "in-train" only of the recurrence interval (λ*) over thickness of deformation (H), thought to be the representation of the λ/d ratio. Large ratios likely represent harmonics (see Fig 9).

90x177mm (300 x 300 DPI)

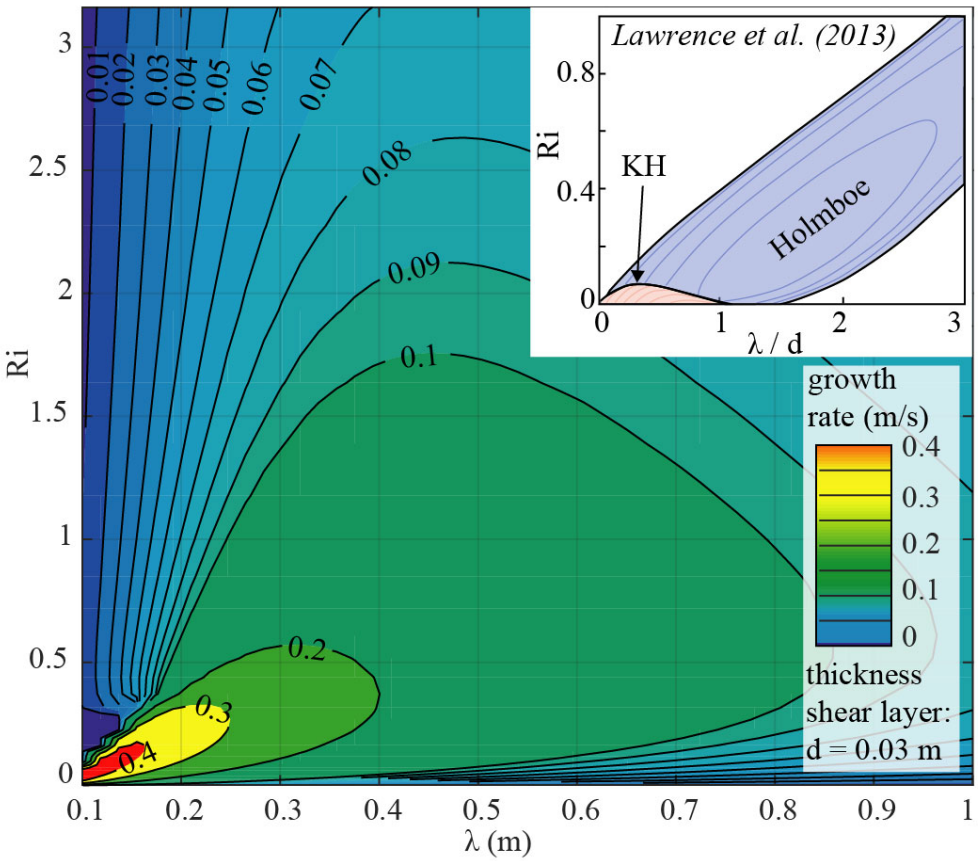

Gradient density model. Growth rate of the perturbation as a function of the Richardson number (Ri) and wavelength for a thickness of shear layer d = 3 cm. Inset: Comparison of the maximal growth zones for Kelvin-Helmholtz (KH, red) and Holmboe (blue) instabilities, redrawn from figure 5.3 in Lawrence et al. (2013).

90x77mm (300 x 300 DPI)

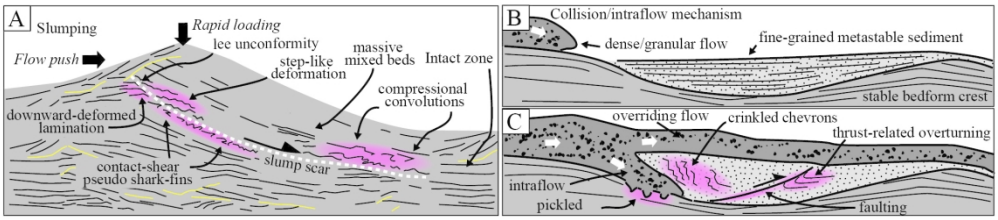

Interpretative sketches for the alternative explanations. A) the slumping mechanism for the lunate outcrop. B) and C) The mechanism of deformation forming the sediment-dike via the intrusion of a dense granular flow within fine-grained metastable sediment.

180x39mm (300 x 300 DPI)

Annex 2

Stability of a wavy interface at a shear horizon

1. Setting

1.1. Initial configuration

The problem is considered in 2 dimensions (the vertical $\mathbf{e_z}$ and the horizontal flow direction $\mathbf{e_x}$). Two semi-infinite, incompressible fluids of constant velocity $\mathbf{U_0}$ are linked by a shear horizon of thickness *2*d* centered around *z=0* with linear velocity profile such as (Fig 12):

$$\overline{\boldsymbol{U_x}(z)} = \begin{cases} U_0 if z > d \\ -U_0 if z < -d \\ \frac{z}{d} . U_0 if |z| < d \end{cases} \quad (1)$$

The mediums are considered incompressible and with density $\overline{\rho}(z)$, that is taken constant in one case (Chapter 2). In a second case, density is linearly decreasing with height and separated by a shear horizon with constant density (Chapter 3).

1.2 Perturbations

The interfaces of the shear horizon are subjected to a sinusoidal perturbation η around their initial position:

$$\begin{aligned} \eta^+(x,t) &= \hat{\eta^+} . e^{i(kx - wt)} \text{around} z = d \\ \eta^-(x,t) &= \hat{\eta^-} . e^{i(kx - wt)} \text{around} z = -d \end{aligned} \quad (2)$$

With $\hat{\eta^+}$ and $\hat{\eta^-}$ the amplitudes of the perturbations.

It follows that the velocity $\boldsymbol{U}$, the fluid pressure P, and the fluid density ρ will deviate from their initial state, the resulting variables being written as the sum of the initial field $\left(\overline{\boldsymbol{U}}, \overline{\rho}, \overline{P}\right)$ and perturbations $(\boldsymbol{u'}, \rho', p')$:

$$\begin{aligned} \boldsymbol{U} &= \overline{\boldsymbol{U}} + \boldsymbol{u'} \\ \rho &= \overline{\rho} + \rho' \quad (3) \\ P &= \overline{P} + p' \end{aligned}$$

With $\boldsymbol{U}(x,z,t) = \begin{pmatrix} U_{x(x,z,t)} \\ U_z(x,z,t) \end{pmatrix}$, $\overline{\boldsymbol{U}} = \begin{pmatrix} \overline{U_x(z)} \\ 0 \end{pmatrix}$ and $\boldsymbol{u'} = \begin{pmatrix} u_{x'}(x,z,t) \\ u_z'(x,z,t) \end{pmatrix}$.

1.4 Constitutive equations

(1) The conservation of momentum for an inviscid fluid solely driven by gravity is:

$$\begin{aligned} \frac{d\rho \boldsymbol{U}}{dt} &= \rho . \frac{d\boldsymbol{U}}{dt} + \boldsymbol{U} . \frac{d\rho}{dt} \\ \frac{d\rho \boldsymbol{U}}{dt} &= \rho . \vec{g} - \overrightarrow{grad}(P) \end{aligned} \quad (4)$$

with $\vec{g} = \begin{pmatrix} 0 \\ -g \end{pmatrix}$ the gravity acceleration.

(2) The mass conservation yields to the continuity equation:

$$\frac{\partial \rho}{\partial t} + div\left(\rho . \boldsymbol{U}\right) = 0 \quad (5)$$

(3) The assumption of incompressibility entrains that the total derivative of the density (the variations following a volume of fluid) has to be zero. This means that density changes can be advected but not diffused, i.e:

$$\frac{D\rho}{Dt} = 0 \leftrightarrow \frac{\partial \rho}{\partial t} + \boldsymbol{U} . \overrightarrow{grad}\left(\rho\right) = 0 \quad (6)$$

Finally, combining the incompressibility (6) and continuity equations (5) for a non-zero density yields:

$$Div(\boldsymbol{U}) = 0 \leftrightarrow \frac{\partial U_x}{\partial x} + \frac{\partial U_z}{\partial z} = 0 \quad (7)$$

This expressions shows that the velocity can be written as deriving from a potential, yet this implies an irrotational flow.

1.5. Boundary conditions

In order to resolve the problem, several boundary conditions are involved.

1.5.1. Finite perturbations

The perturbation of the interfaces is considered as having a finite influence, so that its effect far away from the interfaces is vanishing. Concretely, this means that any effect should vanish with $z => \pm \infty$.

1.5.2. Continuity of the vertical velocity at the interfaces

-The fluid particles at the interfaces of the shear horizon in $z = d + \eta^+$ and $z = -d + \eta^-$ must move with the interfaces, avoiding collocations of two fluids at the same time, as well as cavitation formed between the fluids. This condition is translated into the following equations:

at $z = d + \eta^+$

$$\begin{aligned} \frac{D\eta^+}{Dt} &= \frac{\partial \eta^+}{\partial t} + U_x\left(z = d^+ + \eta^+\right) . \frac{\partial \eta^+}{\partial x} = U_z\left(z = d^+ + \eta^+\right) \\ \frac{D\eta^+}{Dt} &= \frac{\partial \eta^+}{\partial t} + U_x\left(z = d^- + \eta^+\right) . \frac{\partial \eta^+}{\partial x} = U_z\left(z = d^- + \eta^+\right) \end{aligned} \quad (8)$$

at $z = -d + \eta^-$

$$\begin{aligned} \frac{D\eta^-}{Dt} &= \frac{\partial \eta^-}{\partial t} + U_x\left(z = -d^+ + \eta^-\right) . \frac{\partial \eta^-}{\partial x} = U_z\left(z = -d^+ + \eta^-\right) \\ \frac{D\eta^-}{Dt} &= \frac{\partial \eta^-}{\partial t} + U_x\left(z = -d^- + \eta^-\right) . \frac{\partial \eta^-}{\partial x} = U_z\left(z = -d^- + \eta\right) \end{aligned} \quad (9)$$

1.5.3. Continuity of the pressure at the interfaces

At an interface with negligible thickness, the continuity principle states that the fluid pressure at both sides of the interface should be equal. As the initial pressure field is continuous, the perturbed term *p'* is continuous too:

$$p'\left(z = d^+ + \eta^+\right) = p'\left(z = d^- + \eta^+\right) and p'\left(z = -d^+ + \eta^-\right) = p'\left(z = -d^- + \eta^-\right) \quad (10)$$

With all these conditions, the problem is now fully posed in terms of physics, and can be resolved. In the following, we develop two examples of analytic mathematical resolutions. The first model considers two mediums of constant and similar density. The second one considers two flows with a linear density gradient decreasing with height. The shear horizon is considered as a mixing zone with an averaged and constant density.

1.6. Assumptions of small variations and small perturbations

Common assumptions are made on the quantities of the problem for linearization of constitutive equations:

(1). Oscillations of the interfaces only generate weak perturbations on the velocity field and its derivatives compared to the flow velocity, i.e.:

$$\boldsymbol{u'} \ll \boldsymbol{U}$$

$$\frac{\partial \boldsymbol{u'}}{\partial x} \ll \boldsymbol{U} and \frac{\partial \boldsymbol{u'}}{\partial z} \ll \boldsymbol{U} and \frac{\partial \boldsymbol{u'}}{\partial t} \ll \boldsymbol{U}$$

(2). Pressure fluctuations are weak compared to the pressure field:

$$p' \ll \overline{P}$$

(3*) Further, the Boussinesq approximation will be used for the case of a non-constant density (see chapter 4).

2. Resolution for two flows with constant density

In our first case, the density is considered as a constant value ρ_0 for the whole system.

A set of three equations now controls the evolution of the perturbed flow:

$$\begin{aligned} \frac{\partial U_x}{\partial t} + U_x . \frac{\partial U_x}{\partial x} + U_z . \frac{\partial U_x}{\partial z} &= -\frac{1}{\rho_0} . \frac{\partial P}{\partial x} \\ \frac{\partial U_z}{\partial t} + U_x . \frac{\partial U_z}{\partial x} + U_z . \frac{\partial U_z}{\partial z} &= -g - \frac{1}{\rho_0} . \frac{\partial P}{\partial z} \\ \frac{\partial U_x}{\partial x} + \frac{\partial U_z}{\partial z} &= 0 \end{aligned} \quad (11)$$

Since the initial flow should obey the constitutive equations, and given that the vertical velocity of the initial flow is null, $\bar{U}$ is ruled by:

$$\frac{\partial \overline{U_x}}{\partial t} + \overline{U_x} \cdot \frac{\partial \overline{U_x}}{\partial x} + \overline{U_z} \cdot \frac{\partial \overline{U_x}}{\partial z} = -\frac{1}{\overline{\rho_0}} \cdot \frac{\partial \overline{P}}{\partial x} (12a)$$

$$g = -\frac{1}{\overline{\rho_0}} \cdot \frac{\partial \overline{P}}{\partial z} (12b)$$

$$\frac{\partial \overline{U_x}}{\partial x} = 0 (12c)$$

Equation (12c)is also a natural consequence of the initial problem being posed without an horizontal length scale.

Substituting the expression of the perturbed values into (11) and considering the first-order approximations (7, 8, 9), as well as using the equations of the initial flow (12), it results a set of perturbation equations with the following form:

$$\frac{\partial u_x'}{\partial t} + \overline{U_x} \cdot \frac{\partial u_x'}{\partial x} + u_z' \cdot \frac{\partial \overline{U_x}}{\partial z} = -\frac{1}{\rho_0} \frac{\partial p'}{\partial x} (13a)$$

$$\frac{\partial u_z'}{\partial t} + \overline{U_x} \cdot \frac{\partial u_z'}{\partial x} = -g - \frac{1}{\rho_0} \frac{\partial p'}{\partial z} (13b)$$

$$\frac{\partial u_x'}{\partial x} + \frac{\partial u_z'}{\partial z} = 0 (13c)$$

2.1. Establishing the Rayleigh equation

Differentiating (13a) with respect to z and (13b) with respect to x yields:

$$\frac{\partial^2 u_x'}{\partial t \partial z} + \frac{\partial \overline{U_x}}{\partial z} \cdot \frac{\partial u_x'}{\partial x} + \overline{U_x} \cdot \frac{\partial^2 u_x'}{\partial x \partial z} + \frac{\partial u_z'}{\partial z} \cdot \frac{\partial \overline{U_x}}{\partial z} + u_z' \cdot \frac{\partial^2 \overline{U_x}}{\partial z^2} = -\frac{1}{\rho_0} \frac{\partial^2 p'}{\partial x \partial z} (14a)$$

$$\frac{\partial^2 u_z'}{\partial t \partial x} + \frac{\partial \overline{U_x}}{\partial x} \cdot \frac{\partial u_z'}{\partial x} + \overline{U_x} \cdot \frac{\partial^2 u_z'}{\partial x^2} = -\frac{1}{\rho_0} \frac{\partial^2 p'}{\partial z \partial x} (14b)$$

Adding (14a) and (14b) eliminates the pressure terms in an expression rewritten as:

$$\frac{\partial^2 u_x'}{\partial t \partial z} + \frac{\partial \overline{U_x}}{\partial z} \cdot \frac{\partial u_x'}{\partial x} + \overline{U_x} \cdot \frac{\partial^2 u_x'}{\partial x \partial z} + \frac{\partial u_z'}{\partial z} \cdot \frac{\partial \overline{U_x}}{\partial z} + u_z' \cdot \frac{\partial^2 \overline{U_x}}{\partial z^2} = \frac{\partial^2 u_z'}{\partial t \partial x} + \frac{\partial \overline{U_x}}{\partial x} \cdot \frac{\partial u_z'}{\partial x} + \overline{U_x} \cdot \frac{\partial^2 u_z'}{\partial x^2} (15)$$

The perturbed velocity satisfies the incompressibility equation (13c) so that we can define a stream function such as:

$$u_x' = \frac{\partial \varphi}{\partial z}$$
$$u_z' = -\frac{\partial \varphi}{\partial x} (16)$$

with φ the perturbed potential associated with the velocity perturbation. Note that this implies that the flow is irrotational.

Introducing these expressions (16) into (15) yields:

$$\frac{\partial^3 \varphi}{\partial t \partial z^2} + \frac{\partial \overline{U_x}}{\partial z} \cdot \frac{\partial^2 \varphi}{\partial x \partial z} + \overline{U_x} \cdot \frac{\partial^3 \varphi}{\partial x \partial z^2} - \frac{\partial^2 \varphi}{\partial z \partial x} \cdot \frac{\partial \overline{U_x}}{\partial z} - \frac{\partial \varphi}{\partial x} \cdot \frac{\partial^2 \overline{U_x}}{\partial z^2} = \frac{\partial^3 \varphi}{\partial t \partial x^2} - \frac{\partial \overline{U_x}}{\partial x} \cdot \frac{\partial^2 \varphi}{\partial x^2} - \overline{U_x} \cdot \frac{\partial^3 \varphi}{\partial x^3} (16)$$

This expression shows that φ and p' are solutions of coupled equations with coefficients only involving the z coordinate. Solutions for such equations are normal modes in the form:

$$\varphi = \hat{\varphi} \cdot e^{i(kx - wt)}$$
$$p' = \hat{p'} \cdot e^{i(kx - wt)} (17)$$

where $\hat{\varphi}$ and $\hat{p'}$ are the z-dependent amplitudes of perturbations on the velocity potential and the fluid pressure, respectively.

The wave velocity is defined as:

$$c = \frac{w}{k} \quad (18)$$

Using (18) and substituting (17) into (16) yields, after division by $i \cdot k$:

$$k^2 \cdot c \cdot \hat{\varphi} - c \frac{\partial^2 \hat{\varphi}}{\partial z^2} - \overline{U_x} \cdot k^2 \cdot \hat{\varphi} + \overline{U_x} \cdot \frac{\partial^2 \hat{\varphi}}{\partial z^2} - \frac{\partial^2 \overline{U_x}}{\partial z^2} \cdot \hat{\varphi} = 0 \quad (19)$$

Rearranging the terms and dividing by $\left(\frac{1}{\left(\overline{U_x} - c\right)}\right)$ yields the Rayleigh equation:

$$\frac{d^2\hat{\varphi}}{dz^2} - \left[\frac{1}{\left(\overline{U_x} - c\right)} . \frac{d^2\overline{U_x}}{dz^2} + k^2\right] . \hat{\varphi} = 0 (20)$$

2.2. Resolution of the Rayleigh equation for the perturbed flow

2.2.1. The specific case of piecewise linear profiles of fluid velocity

Usually, the resolution of the Rayleigh equation is complicated, but the geometry of the problem with piecewise linear profiles of velocity and density enables to find an analytical solution. The initial flow is linear apart at shear interfaces, i.e.:

$$\frac{d^2\overline{U_x}}{dz^2} = 0 \, for \, \left|z\right| < d \, and \, for \, \left|z\right| > d$$

Within the three domains, the Taylor-Goldstein equation simplifies into an ordinary second-order differential equation:

$$\frac{d^2\hat{\varphi}}{dz^2} - k^2 . \hat{\varphi} = 0 (21)$$

With a well-established solution given by:

$$\hat{\varphi} = \begin{cases} B_+ . e^{-kz} for z > d \\ A_- . e^{kz} for z < -d \\ A . e^{kz} + B . e^{-kz} for \left|z\right| < d \end{cases} \quad (22)$$

Note that we omitted the increasing exponentials of the general solution because the perturbation should vanish away from the interfaces (boundary condition 1.5.1).

2.2.2. Continuity of the vertical velocity at the interfaces

In order to find the dispersion equation of the pulsation *w* as a function of k, the constants (B_+, A, B, A_-)must be constrained. Recall the property of the continuity of the normal velocity at the interfaces $z = d + \eta^+$ and $z = -d + \eta^-$ (boundary condition 1.5.2).

By substituting the expressions of U_x, U_z, η^+, η^- and u_z' and neglecting the second-order terms, a linearized system is obtained:

at $z = d + \eta^+$

$$\begin{aligned} -c . \eta^+ + U_0 . \eta^+ &= B^+ . e^{-\alpha d} \\ -c . \eta^+ + U_0 . \eta^+ &= A . e^{kd} + B . e^{-kd} \end{aligned} (23a)$$

at $z = -d + \eta^-$

$$\begin{aligned} -c . \eta^- + U_0 . \eta^- &= A . e^{-kd} + B . e^{kd} \\ -c . \eta^+ + U_0 . \eta^+ &= A^- . e^{-\alpha d} \end{aligned} (23b)$$

And by combining side by side equations (23a) and (23b), two relationships between the constants (B_+, A, B, A_-) are obtained:

$$\begin{aligned} B^+ &= \left(A . e^{kd} + B . e^{-kd}\right) . e^{\alpha d} \\ A^- &= \left(A . e^{-kd} + B . e^{kd}\right) . e^{-\alpha d} \end{aligned} (24)$$

So that (22) becomes:

$$\hat{\varphi} = \begin{cases} \left(A . e^{kd} + B . e^{-kd}\right) . e^{\alpha d} . e^{-\alpha z} for z > d \\ \left(A . e^{-kd} + B . e^{kd}\right) . e^{-\alpha d} . e^{\alpha z} for z < -d \\ A . e^{kz} + B . e^{-kz} for \left|z\right| < d \end{cases} (25)$$

2.2.3. Continuity of the pressure at the interfaces

A relationship between $\hat{\varphi}$ and $\hat{p'}$ is established by introducing the expressions of p', u_1' and u_2' into the Momentum equation (11):

$$\left(\overline{U_x} - c\right) . \frac{\partial\hat{\varphi}}{\partial z} - \frac{\partial\overline{U_x}}{\partial z} . \hat{\varphi} = \frac{1}{\rho_0} . \hat{p'} (26)$$

Given that pressure shall be continuous at the interface (boundary condition 1.5.3), it follows from (26) that the quantity $\left(\overline{U_x}-c\right).\frac{\partial\hat{\varphi}}{\partial z}-\frac{\partial\overline{U_x}}{\partial z}.\hat{\varphi}$ also varies continuously at the interfaces. By replacing $\overline{U_x}$ by its expression, the conditions at the interfaces appear as:

- at $z=d+\eta^+$:

$$\left(U_0-c\right).\frac{\partial\hat{\varphi}}{\partial z}\Big|_{d^++\eta^+}+0.\hat{\varphi}\Big|_{d^++\eta^+}=\left(U_0-c\right).\frac{\partial\hat{\varphi}}{\partial z}\Big|_{d^-+\eta^+}-\frac{U_0}{d}.\hat{\varphi}_{d^-+\eta^+}(27a)$$

- at $z=-d+\eta^-$:

$$\left(-U_0-c\right).\frac{\partial\hat{\varphi}}{\partial z}\Big|_{-d^++\eta^-}-\frac{U_0}{d}.\hat{\varphi}\Big|_{-d^++\eta^-}=\left(-U_0-c\right).\frac{\partial\hat{\varphi}}{\partial z}\Big|_{-d^-+\eta^-}-0.\hat{\varphi}\Big|_{-d^-+\eta^-}(27b)$$

Introducing the expression of $\hat{\varphi}$ given by (25) into (27a) and (27b) gives a new relationship between the constants A and B:

- At $z=d+\eta^+$:

$$k.\left(c-U_0\right).\left(A.e^{kd}+B.e^{-kd}\right)=k.\left(U_0-c\right).\left(A.e^{kd}-B.e^{-kd}\right)-\frac{U_0}{d}.\left(A.e^{kd}+B.e^{-kd}\right)(28a)$$

- At $z=-d+\eta^-$:

$$-k.\left(U_0+c\right).\left(A.e^{-kd}-B.e^{kd}\right)-\frac{U_0}{d}.\left(A.e^{-kd}+B.e^{kd}\right)=-k.\left(U_0+c\right).\left(A.e^{-kd}+B.e^{kd}\right)(28b)$$

Rearranging the terms of (28a) and (27a) yields the system:

$$\begin{matrix}\left[2k\left(c-U_0\right)+\frac{U_0}{d}\right].A+\left[\frac{U_0}{d}.e^{-2kd}\right].B=0\\ \left[-\frac{U_0}{d}.e^{-2kd}\right].A+\left[2k\left(U_0+c\right)-\frac{U_0}{d}\right].B=0\end{matrix}\quad(29)$$

2.3. Finding the dispersion equation for the perturbation

The previous system has a non-trivial solution if the determinant of system (29) is 0, i.e.:

$$\left[2k\left(c-U_0\right)+\frac{U_0}{d}\right].\left[2k\left(U_0+c\right)-\frac{U_0}{d}\right]-\left[\frac{U_0}{d}.e^{-2kd}\right].\left[-\frac{U_0}{d}.e^{-2kd}\right]=0(30)$$

With some rearrangements, (30) is equivalent to:

$$4w^2-4k^2U_0^2+4k\frac{U_0^2}{d}-\frac{U_0^2}{d^2}+\frac{U_0^2}{d^2}.e^{-4kd}=0(31)$$

It corresponds to the dispersion equation for the perturbation: if w is real then the perturbation is a periodic wave, otherwise the perturbation is unstable and its growth rate is given by the imaginary part of w. The roots of this complex equation are found numerically using the Matlab solver “solve” (Fig 13).

3. Case of flows with a linear density gradient

We now consider the case of two flows with a linear density gradient. The shear horizon is considered as a mixing zone with an averaged and constant. The resolution of the dispersed equation follows a similar structure and method as for the constant density.

The initial density profile is defined by:

$$\frac{d\overline{\rho(z)}}{dz}=\begin{cases}sifz>d\\ sifz<-d\\ 0if\left|z\right|<d\end{cases}\quad(32)$$

And the perturbation of the interface entrains perturbation such as:

$$\rho(x,z,t)=\overline{\rho}(z)+\rho'(x,z,t)\ (33)$$

3.1. Linearization

For the case of varying density, the often used Boussinesq approximation is introduced. This approximation considers that the density ρ is the sum of a mean density ρ_0 and a varying term ρ'' that is weak and weakly evolving compared to ρ_0 and the velocity fluctuations:

$$\rho(x,z,t) = \rho_0 + \rho''(x,z,t) with \rho' \ll \rho_0 \quad (34)$$
$$\frac{d\rho}{dt} = \frac{d\rho''}{dt} \ll \frac{d\boldsymbol{U}}{dt}$$

It results that we ignore the products of ρ'' with small quantities, as well as any derivative of ρ'' so that, (9a) simplifies into:

$$\frac{d\rho\boldsymbol{U}}{dt} = (\rho_0 + \rho'') . \frac{d\boldsymbol{U}}{dt} + U . \frac{d\rho''}{dt} \cong \rho_0 . \frac{d\boldsymbol{U}}{dt} \quad (35)$$

Thus, equalizing (10) and (9b) and developing $\frac{d\boldsymbol{U}}{dt}$ yields:

$$\rho_0 . \left[\frac{\partial \boldsymbol{U}}{\partial t} + \left(\boldsymbol{U} . \overrightarrow{\text{grad}} \right) . \boldsymbol{U} \right] = \rho . \vec{\boldsymbol{g}} - \overrightarrow{grad}(P) \quad (36)$$

so that density fluctuations in (36) are only accounted for in the buoyancy $\rho . \vec{\boldsymbol{g}}$, all other occurrences of ρ being approximated as ρ_0.

Since the initial flow should obey this modified equation of momentum (36), $\overline{\boldsymbol{U}}$ in (1) and $\overline{\rho}$ in (32) shall satisfy on both space directions:

$$\frac{\partial \overline{U_x}}{\partial t} + \overline{U_x} . \frac{\partial \overline{U_x}}{\partial x} + \overline{U_z} . \frac{\partial \overline{U_x}}{\partial z} = -\frac{1}{\rho_0} . \frac{\partial \overline{P}}{\partial x}$$
$$\frac{\partial \overline{U_z}}{\partial t} + \overline{U_x} . \frac{\partial \overline{U_z}}{\partial x} + \overline{U_z} . \frac{\partial \overline{U_z}}{\partial z} + \frac{\overline{\rho}}{\rho_0} . g = -\frac{1}{\rho_0} . \frac{\partial \overline{P}}{\partial z} \quad (37)$$

Similarly, the initial flow is incompressible (7) and the vertical velocity of the initial flow is null, so that:

$$\frac{\partial \overline{U_x}}{\partial x} = 0 \quad (38)$$

This latter equality is also a natural consequence of the initial problem being posed without horizontal length scale.

A set of four equations now controls the evolution of the perturbed flow:

$$\frac{\partial U_x}{\partial t} + U_x . \frac{\partial U_x}{\partial x} + U_z . \frac{\partial U_x}{\partial z} = -\frac{1}{\rho_0} . \frac{\partial P}{\partial x}$$
$$\frac{\partial U_z}{\partial t} + U_x . \frac{\partial U_z}{\partial x} + U_z . \frac{\partial U_z}{\partial z} = -\frac{\rho}{\rho_0} . g - \frac{1}{\rho_0} . \frac{\partial P}{\partial z} \quad (39)$$
$$\frac{\partial \rho}{\partial t} + div\left(\rho . \boldsymbol{U}\right) = 0$$
$$\frac{\partial U_x}{\partial x} + \frac{\partial U_z}{\partial z} = 0$$

Substituting the expressions of the perturbed state into (39), and simplifying with the first order approximations, removing terms that are zero by definition, and using the relations on the initial flow (37 and 38), the system translates as:

$$\frac{\partial u_x'}{\partial t} + \overline{U_x} . \frac{\partial u_x'}{\partial x} + u_z' . \frac{\partial \overline{U_x}}{\partial z} = -\frac{1}{\rho_0} \frac{\partial p'}{\partial x} \quad (40a)$$
$$\frac{\partial u_z'}{\partial t} + \overline{U_x} . \frac{\partial u_z'}{\partial x} = -\frac{\rho'}{\rho_0} . g - \frac{1}{\rho_0} \frac{\partial p'}{\partial z} \quad (40b)$$
$$\frac{\partial \rho'}{\partial t} + \overline{\rho} . \frac{\partial u_x'}{\partial t} + \overline{U_x} . \frac{\partial \rho'}{\partial x} + u_z' . \frac{\partial \overline{\rho}}{\partial z} + \overline{\rho} . \frac{\partial u_z'}{\partial z} = 0 \quad (40c)$$
$$\frac{\partial u_x'}{\partial x} + \frac{\partial u_z'}{\partial z} = 0 \quad (40d)$$

3.2. Establishing the Taylor Goldstein equation

Differentiating (40a) with respect to *z* and (40b) with respect to *x* yields:

$$\frac{\partial^2 u_x'}{\partial t\,\partial z} + \frac{\partial \overline{U_x}}{\partial z}\cdot\frac{\partial u_x'}{\partial x} + \overline{U_x}\cdot\frac{\partial^2 u_x'}{\partial x\,\partial z} + \frac{\partial u_z'}{\partial z}\cdot\frac{\partial \overline{U_x}}{\partial z} + u_z'\cdot\frac{\partial^2 \overline{U_x}}{\partial z^2} = -\frac{1}{\rho_0}\frac{\partial^2 p'}{\partial x\,\partial z} \quad (41a)$$

$$\frac{\partial^2 u_z'}{\partial t\,\partial x} + \overline{U_x}\cdot\frac{\partial^2 u_z'}{\partial x^2} - \frac{g}{\rho_0}\cdot\frac{\partial \rho'}{\partial x} = -\frac{1}{\rho_0}\frac{\partial^2 p'}{\partial z\,\partial x} \quad (41b)$$

Adding (41a) and (41b) eliminates the pressure terms in an expression rewritten as:

$$\frac{\partial^2 u_x'}{\partial t\,\partial z} + \frac{\partial \overline{U_x}}{\partial z}\cdot\frac{\partial u_x'}{\partial x} + \overline{U_x}\cdot\frac{\partial^2 u_x'}{\partial x\,\partial z} + \frac{\partial u_z'}{\partial z}\cdot\frac{\partial \overline{U_x}}{\partial z} + u_z'\cdot\frac{\partial^2 \overline{U_x}}{\partial z^2} = \frac{\partial^2 u_z'}{\partial t\,\partial x} + \overline{U_x}\cdot\frac{\partial^2 u_z'}{\partial x^2} - \frac{g}{\rho_0}\cdot\frac{\partial \rho'}{\partial x} \quad (42)$$

A stream function is defined for the perturbation, which satisfies the incompressibility equation (40d):

$$u_x' = \frac{\partial \varphi}{\partial z}$$
$$u_z' = -\frac{\partial \varphi}{\partial x} \quad (43)$$

with φ the perturbed potential associated to the velocity perturbation.

Introducing the stream function (43) into (42) yields:

$$\frac{\partial^3 \varphi}{\partial t\,\partial z^2} + \frac{\partial \overline{U_x}}{\partial z}\cdot\frac{\partial^2 \varphi}{\partial x\,\partial z} + \overline{U_x}\cdot\frac{\partial^3 \varphi}{\partial x\,\partial z^2} - \frac{\partial^2 \varphi}{\partial z\,\partial x}\cdot\frac{\partial \overline{U_x}}{\partial z} - \frac{\partial \varphi}{\partial x}\cdot\frac{\partial^2 \overline{U_x}}{\partial z^2} = -\frac{\partial^3 \varphi}{\partial t\,\partial x^2} - \overline{U_x}\cdot\frac{\partial^3 \varphi}{\partial x^3} - \frac{g}{\rho_0}\cdot\frac{\partial \rho'}{\partial x} \quad (44)$$

ρ' and p' are thus solutions of coupled equations with coefficients only involving the z coordinate. Solutions of such systems are normal modes of the form:

$$\varphi = \hat{\varphi}(z)\cdot e^{i(kx-wt)}$$
$$\rho' = \hat{\rho'}(z)\cdot e^{i(kx-wt)} \quad (45)$$
$$p' = \hat{p'}(z)\cdot e^{i(kx-wt)}$$

where $\hat{\varphi}$, $\hat{\rho'}$, and $\hat{p'}$ are the amplitudes of perturbations on the potential, fluid density, and fluid pressure, respectively.

The wave velocity is defined as:

$$c = \frac{w}{k} \quad (46)$$

Substituting (45) into (44) and using (46) yields:

$$k^2\cdot c\cdot\hat{\varphi} - c\cdot\frac{\partial^2 \hat{\varphi}}{\partial z^2} - \overline{U_x}\cdot k^2\cdot\hat{\varphi} + \overline{U_x}\cdot\frac{\partial^2 \hat{\varphi}}{\partial z^2} - \frac{\partial^2 \overline{U_x}}{\partial z^2}\cdot\hat{\varphi} = \frac{g}{\rho_0}\cdot\hat{\rho'} \quad (47)$$

Similarly, replacing the expressions of (45) in (40c) allow to identify $\hat{\rho'}$ as a function of $\hat{\varphi}$ and of the initial flow density profile $\frac{\partial \overline{\rho}}{\partial z}$:

$$(\overline{U_x} - c)\cdot\hat{\rho'} = -\hat{\varphi}\cdot\frac{\partial \overline{\rho}}{\partial z} \quad (48)$$

Combining (48) and (46) results in the Taylor-Goldstein equation:

$$\frac{\partial^2 \hat{\varphi}}{\partial z^2} + \left[\frac{N^2}{\left(\overline{U_x} - c\right)^2} - \frac{1}{\overline{U_x} - c}\cdot\frac{\partial^2 \overline{U_x}}{\partial z^2} - k^2\right]\cdot\hat{\varphi} = 0 \quad (49a)$$

With N^2 the buoyancy frequency (or Brunt-Väisälä frequency) defined as:

$$N^2 = -\frac{g}{\rho_0}\cdot\frac{d\overline{\rho}}{dz} \quad (49b)$$

N^2 is a value describing the degree of stratification of the medium: fluids with strong vertical density gradient will be characterized by a high value of N^2.

3.3. Resolution of the Taylor-Goldstein equation for the initial flow

3.3.1. Piecewise linear profiles of density and velocity

As for the Rayleigh equation, the resolution of the Taylor-Goldstein equation is usually complicated but tackled analytically here via the piecewise linear profiles of velocity and density. The medium is split again so that:

$$\begin{matrix} \frac{\partial^2 \overline{U_x}}{\partial z^2} = 0 \\ N^2 = 0 \end{matrix} \text{ for } |z| < d (50a)$$

and

$$\begin{matrix} \frac{\partial^2 \overline{U_x}}{\partial z^2} = 0 \\ N^2 = N_0 = constant \end{matrix} \text{ for } |z| > d (50b)$$

Within both domains, the Taylor-Goldstein equation simplifies to the following ordinary second-order differential equation:

$$\frac{d^2 \hat{\varphi}}{dz^2} + \alpha^2 . \hat{\varphi} = 0 (51a)$$

with:

$$\alpha^2 = \begin{cases} -k^2 for |z| < d \\ \frac{{N_0}^2}{(\overline{U_x} - c)^2} for |z| > d \end{cases} (51b)$$

The solution to such an ordinary differential equation (51a, 51b) is of the form:

$$\hat{\varphi} = \begin{cases} B_+ . e^{-\alpha z} for z > d \\ A_- . e^{\alpha z} for z < -d \\ A . e^{kz} + B . e^{-kz} for |z| < d \end{cases} (52)$$

Again, the constant involving the exponential increasing for $z => \pm \infty$ are omitted because the perturbation is finite (boundary condition 1.5.1.).

In order to find the dispersion equation of the wave number w as a function of k, the constants (B_+, A, B, A_-) are again constrained through the boundary conditions of the normal velocity and pressure at the interfaces $z = d + \eta^+$ and $z = -d + \eta^-$.

3.3.2. Continuity of the vertical velocity at the interfaces

The fluid particles at the interfaces move with the interfaces (boundary condition 1.5.2.).

Introducing $U_x = \overline{U_x} + {u_x}'$ and $U_z = \overline{U_z} + {u_z}'$ for this condition, and neglecting the second-order terms, we obtain the following linearized system:

at $z = d + \eta^+$

$$\begin{matrix} \frac{\partial \eta^+}{\partial t} + U_0 . \frac{\partial \eta^+}{\partial x} = {u_z}'(z = d^+ + \eta^+) \\ \frac{\partial \eta^+}{\partial t} + U_0 . \frac{\partial \eta^+}{\partial x} = {u_z}'(z = d^- + \eta^+) \end{matrix} (53a)$$

at $z = -d + \eta^-$

$$\begin{matrix} \frac{\partial \eta^-}{\partial t} - U_0 . \frac{\partial \eta^-}{\partial x} = {u_z}'(z = -d^+ + \eta^-) \\ \frac{\partial \eta^-}{\partial t} - U_0 . \frac{\partial \eta^-}{\partial x} = {u_z}'(z = -d^- + \eta^-) \end{matrix} (53b)$$

Substituting the expressions of η^+, η^- and ${u_2}'$ in (53a) and (53b) yields:

at $z = d + \eta^+$

$$\begin{matrix} -c . \eta^+ + U_0 . \eta^+ = B^+ . e^{-\alpha d} \\ -c . \eta^+ + U_0 . \eta^+ = A . e^{kd} + B . e^{-kd} \end{matrix} (54a)$$

- at $z = -d + \eta^-$

$$\begin{matrix} -c . \eta^- + U_0 . \eta^- = A . e^{-kd} + B . e^{kd} \\ -c . \eta^+ + U_0 . \eta^+ = A^- . e^{-\alpha d} \end{matrix} (54b)$$

Therefore, adding side by side (54a) and (54b) gives two relationships between the constants:

$$\begin{matrix} B^+ = \left(A . e^{kd} + B . e^{-kd}\right) . e^{\alpha d} \\ A^- = \left(A . e^{-kd} + B . e^{kd}\right) . e^{-\alpha d} \end{matrix} (55)$$

Thus (38) becomes:

$$\hat{\varphi} = \begin{cases} \left(A \,.\, e^{kd} + B \,.\, e^{-kd}\right) \,.\, e^{\alpha d} \,.\, e^{-\alpha z} for z > d \\ \left(A \,.\, e^{-kd} + B \,.\, e^{kd}\right) \,.\, e^{-\alpha d} \,.\, e^{\alpha z} for z < -d \\ A \,.\, e^{kz} + B \,.\, e^{-kz} for \left|z\right| < d \end{cases} \quad (56)$$

3.3.3. Continuity of the pressure at the interfaces

The relationship between $\hat{\varphi}$ and $\hat{p'}$ is established by introducing the expressions of p', u_x' and u_z' into the momentum equation (24a) yields:

$$\left(\overline{U_x} - c\right) \,.\, \frac{\partial \hat{\varphi}}{\partial z} - \frac{\partial \overline{U_x}}{\partial z} \,.\, \hat{\varphi} = \frac{1}{\rho_0} \,.\, \hat{p'} \quad (57)$$

Using the continuity of pressure (boundary condition 1.5.3.), it comes that the quantity $\left(\overline{U_x} - c\right) \,.\, \frac{\partial}{\partial z} - \frac{\partial \overline{U_x}}{\partial z} \,.\, \hat{\varphi}$ varies continuously at the interfaces $z = d + \eta^+$ and $z = -d + \eta^-$. Replacing $\overline{U_x}$ by its expression transforms the conditions at the interfaces in:

at $z = d + \eta^+$:

$$\left(U_0 - c\right) \,.\, \frac{\partial \hat{\varphi}}{\partial z}\bigg|_{d^+ + \eta^+} + 0.\hat{\varphi}\bigg|_{d^+ + \eta^+} = \left(U_0 - c\right) \,.\, \frac{\partial \hat{\varphi}}{\partial z}\bigg|_{d^- + \eta^+} - \frac{U_0}{d} \,.\, \hat{\varphi}_{d^- + \eta^+} \quad (58a)$$

at $z = -d + \eta^-$:

$$\left(-U_0 - c\right) \,.\, \frac{\partial \hat{\varphi}}{\partial z}\bigg|_{-d^+ + \eta^-} - \frac{U_0}{d} \,.\, \hat{\varphi}\bigg|_{-d^+ + \eta^-} = \left(-U_0 - c\right) \,.\, \frac{\partial \hat{\varphi}}{\partial z}\bigg|_{-d^- + \eta^-} - 0.\hat{\varphi}\bigg|_{-d^- + -} \quad (58b)$$

Introducing the expression of $\hat{\varphi}$ given by (46) into (49) and (50) gives a new relationship between the constants A and B:

$$\begin{aligned} &\alpha \,.\, \left(c - U_0\right) \,.\, \left(A \,.\, e^{kd} + B \,.\, e^{-kd}\right) = k \,.\, \left(U_0 - c\right) \,.\, \left(A \,.\, e^{kd} + B \,.\, e^{-kd}\right) - \frac{U_0}{d} \,.\, \left(A \,.\, e^{kd} + B \,.\, e^{-kd}\right) \\ &-k \,.\, \left(U_0 + c\right) \,.\, \left(A \,.\, e^{-kd} + B \,.\, e^{kd}\right) - \frac{U_0}{d} \,.\, \left(A \,.\, e^{-kd} + B \,.\, e^{kd}\right) = \alpha \,.\, \left(U_0 + c\right) \,.\, \left(A \,.\, e^{-kd} + B \,.\, e^{kd}\right) \end{aligned} \quad (59)$$

3.3.4. Finding the dispersion equation for the perturbation

System (59) has a non-trivial solution if the determinant of the system is 0, i.e.:

$$\begin{aligned} &w^3 + \frac{w^2}{2} \,.\, \left(1 + Ri \,.\, e^{2kd}\right) + \frac{w}{2} \,.\, Ri \,.\, \left(e^{2kd} - 1\right) + \frac{Ri}{2} \,.\, sinh^2\left(k \,.\, d\right) = 0 \\ &with Ri = \frac{{N_0}^2 \,.\, d^2}{{U_0}^2} the bulk Richardson number \end{aligned} \quad (60)$$

The bulk Richardson number Ri is a ratio of the buoyancy over the shear forces and it thus quantifies the degree of stratification whereas the non-dimensional ratio $k \,.\, d$ quantifies the ratio between the wavelength of the perturbation and the thickness of the shear horizon.

System (60) corresponds to the dispersion equation for the perturbation: if w is real, the perturbation is a periodic wave, otherwise the perturbation is unstable and its growth rate is given by the imaginary part of w.